Supplementary Information

Topological transformation of microbial proteins into iron single-atom sites for selective hydrogen peroxide electrosynthesis

Xiaofeng Xiao[1, 2*], Zechao Zhuang[3, 4*], Shuhu Yin[5], Jiexin Zhu[6], Tao Gan[7], Ruohan Yu[8], Jinsong Wu[8], Xiaochun Tian[1], Yanxia Jiang[5], Dingsheng Wang[3]✉ and Feng Zhao[1]✉

[1]Key Laboratory of Urban Pollutant Conversion, Institute of Urban Environment, Chinese Academy of Sciences, Xiamen 361021, China

[2]University of Chinese Academy of Sciences, Beijing 100049, China

[3]Department of Chemistry, Tsinghua University, Beijing 100084, China

[4]Department of Chemical Engineering, Columbia University, New York, NY, 10027, USA

[5]College of Chemistry and Chemical Engineering, Discipline of Intelligent Instrument and Equipment, Xiamen University, Xiamen 361005, China

[6]State Key Laboratory of Advanced Technology for Materials Synthesis and Processing, Wuhan University of Technology, Wuhan 430070, China

[7]Shanghai Synchrotron Radiation Facility, Shanghai Advanced Research Institute, Chinese Academy of Sciences, Shanghai 202104, China

[8]Nanostructure Research Centre, Wuhan University of Technology, Wuhan 430070, China

*These authors contributed equally: Xiaofeng Xiao and Zechao Zhuang

✉e-mail: fzhao@iue.ac.cn; wangdingsheng@mail.tsinghua.edu.cn

The **Supporting Information** contains 51 pages, 46 Supplementary figures, 5 tables, and 5 Supplementary References.

Supplementary Figure 1 | RRDE collection efficiency calibration.

Supplementary Figure 2 | ORR electrochemical performances of various microbe-derived carbon materials. **a,** polarization curves for ORR. **b,** Calculated H_2O_2 selectivity. **c,** electron transfer number.

Supplementary Figure 3 | The content of the predominant metal elements in microorganisms (hollow) and the corresponding derived carbon materials (solid fill pattern) measured by ICP-MS.

Supplementary Figure 4 | The STEM image and elemental distribution maps of *Escherichia coli*-derived carbon material.

Supplementary Figure 5 | The STEM image and elemental distribution maps of *Shewanella oneidensis*-derived carbon material.

Supplementary Figure 6 | The STEM image and elemental distribution maps of *Halomonas titanicae*-derived carbon material.

Supplementary Figure 7 | The STEM image and elemental distribution maps of *Pseudomonas aeruginosa*-derived carbon material.

Supplementary Figure 8 | The STEM image and elemental distribution maps of *Cupriavidus necator*-derived carbon material.

Supplementary Figure 9 | The STEM image and elemental distribution maps of *Eubacterium limosum*-derived carbon material.

Supplementary Figure 10 | The STEM image and elemental distribution maps of *Lactobacillus acidophilus*-derived carbon material.

Supplementary Figure 11 | The STEM image and elemental distribution maps of *Bacillus thuringiensis*-derived carbon material.

Supplementary Figure 12 | The STEM image and elemental distribution maps of *Bacillus subtilis*-derived carbon material.

Supplementary Figure 13 | The AC-STEM images and elemental distribution maps of *Bacillus pumilus*-derived carbon material. **a,** Dark field image, **b,** High resolution HAADF-STEM image and **c,** Elemental distribution map.

Supplementary Figure 14 | The STEM image and elemental distribution maps of *Saccharomyces cerevisiae*-derived carbon material.

Supplementary Figure 15 | The morphology of *Bacillus pumilus* and *Bacillus pumilus*(Fe−).

Supplementary Figure 16 | The content of metal elements in *Bacillus pumilus*, *Bacillus pumilus*(Fe−), *Bacillus pumilus*-derived carbon material and *Bacillus pumilus*(Fe−)-derived carbon material.

Supplementary Figure 17 | The STEM and elemental distribution map of *Bacillus pumilus*(Fe−)-derived carbon material.

Supplementary Figure 18 | XPS spectra of *Bacillus pumilus*-derived carbon material (top) and *Bacillus pumilus*(Fe−)-derived carbon material (down).

Supplementary Figure 19 | ORR electrochemical performance of *Bacillus pumilus*-derived carbon material and *Bacillus pumilus*(Fe−)-derived carbon material.

Supplementary Figure 20 | The STEM image and elemental distribution maps of *Bacillus pumilus*-derived carbon material obtained at 450°C.

Supplementary Figure 21 | The STEM image and elemental distribution maps of *Bacillus pumilus*-derived carbon material obtained at 500°C.

Supplementary Figure 22 | The STEM image and elemental distribution maps of *Bacillus pumilus*-derived carbon material obtained at 700°C.

Supplementary Figure 23 | The STEM image and elemental distribution maps of *Bacillus pumilus*-derived carbon material obtained at 900°C.

Supplementary Figure 24 | The specific surface and pore distribution of *Bacillus pumilus-derived carbon materials* obtained at different temperatures.

Supplementary Figure 25 | XPS spectra of *Bacillus pumilus-derived carbon materials* obtained at different tempretures.

Supplementary Figure 26 | Fraction analysis from XPS spectra in *Bacillus pumilus-derived carbon materials* obtained at different tempretures.

Supplementary Figure 27 | XRD patterns of *Bacillus pumilus-derived carbon materials* obtained at different tempretures.

Supplementary Figure 28 | Fe K-edge EXAFS (point) and the curve fit (line) for $FeN_{5-x}O_x$ and FeN_4 catalysts, shown in k^3-weighted *k*-space after Fourier transform (Fourier transform magnitude component).

Supplementary Figure 29 | Fe K-edge EXAFS (point) and the curve fit (line) for $FeN_{5-x}O_x$ and FeN_4 catalysts, shown in k^3-weighted *k*-space after Fourier transform (Fourier transform imaginary component).

Supplementary Figure 30 | Wavelet transform for the k^2-weighted Fe K-edge EXAFS signals of $FeN_{5-x}O_x$ and FeN_4 catalysts.

Supplementary Figure 31 | Schematic of proposed $FeN_{5-x}O_x$ and FeN_4 sites.

Supplementary Figure 32 | ORR intrinsic activity of $FeN_{5-x}O_x$ catalysts.

Supplementary Figure 33 | ORR performance of $FeN_{5-x}O_x$ catalysts in neutral electrolyte.

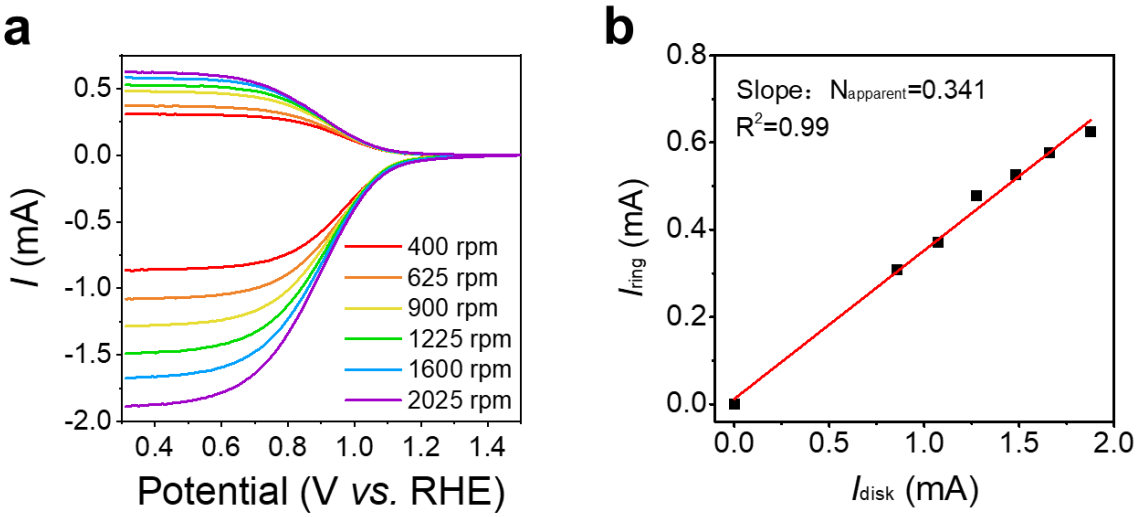

Supplementary Figure 1 | RRDE collection efficiency calibration. a, LSV curves of bare rotating ring-disk electrode at different rotation speed. LSV tested in 0.1 M KOH supporting electrolyte containing 10 mM $K_3Fe(CN)_6$, scan rate: 10 mV s^{-1}, and the potential of ring electrode: 1.55 V *vs*. RHE. **b,** Linear fitting of the diffusion limited current densities collected by ring and disk electrodes. The experimental determined apparent collection efficiency (N) is 34.1% at rotation speed from 400–2025 rpm, and the theoretical vale of 37.0%.

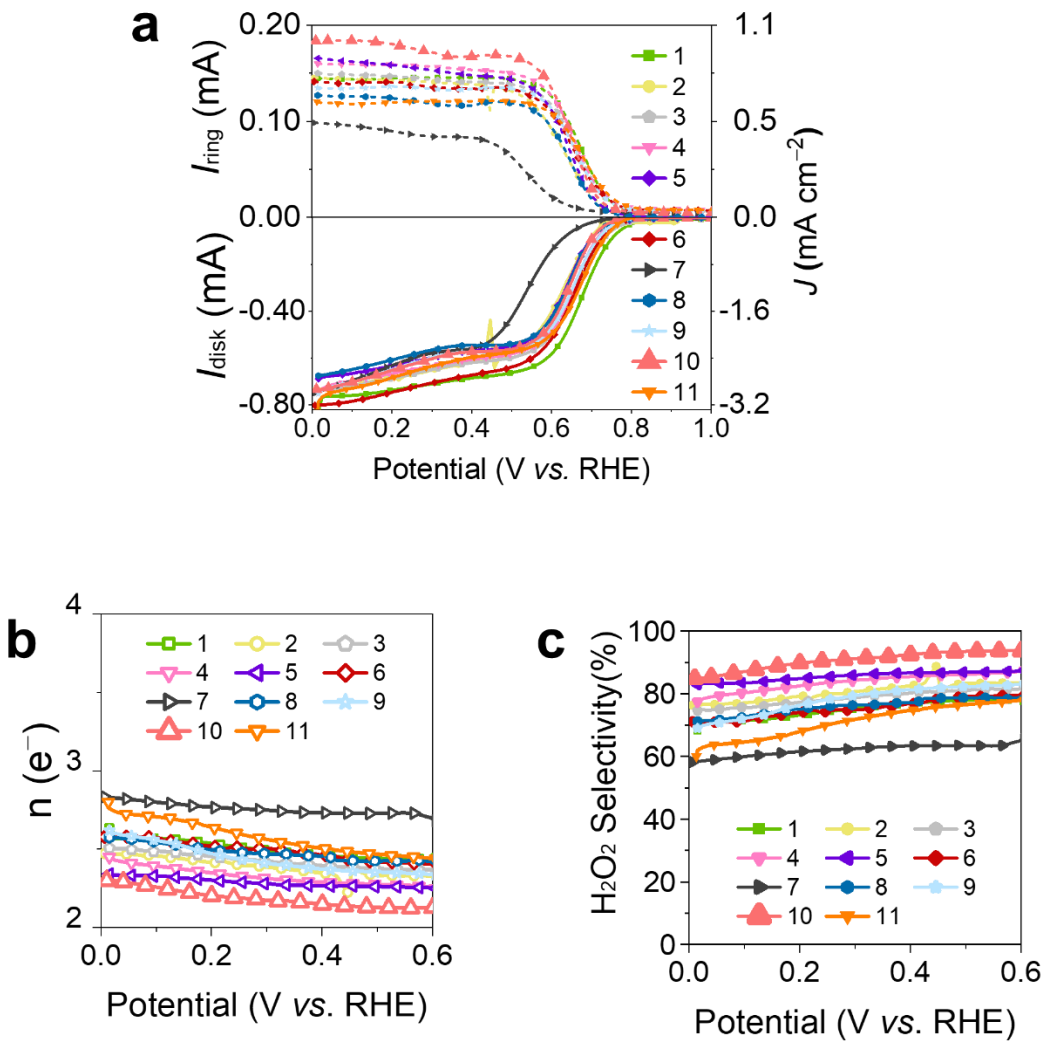

Supplementary Figure 2 | ORR electrochemical performances of various microbe-derived carbon materials. a, polarization curves for ORR. **b,** Calculated H_2O_2 selectivity. **c,** electron transfer number at 0–0.6 V *vs*. RHE. ORR polarization curve measured by a rotating ring-disk electrode at 1600 rpm in O_2-saturated 0.1 M KOH. The absolute mass loading of catalyst on electrode was 0.1 mg cm^{-2}. Numbers 1–11 represent *Escherichia coli*, *Shewanella oneidensis*, *Halomonas titanicae*, *Pseudomonas aeruginosa*, *Cupriavidus necator*, *Eubacterium limosum*, *Lactobacillus acidophilus*, *Bacillus thuringiensis*, *Bacillus subtilis*, *Bacillus pumilus* and *Saccharomyces cerevisiae*, respectively.

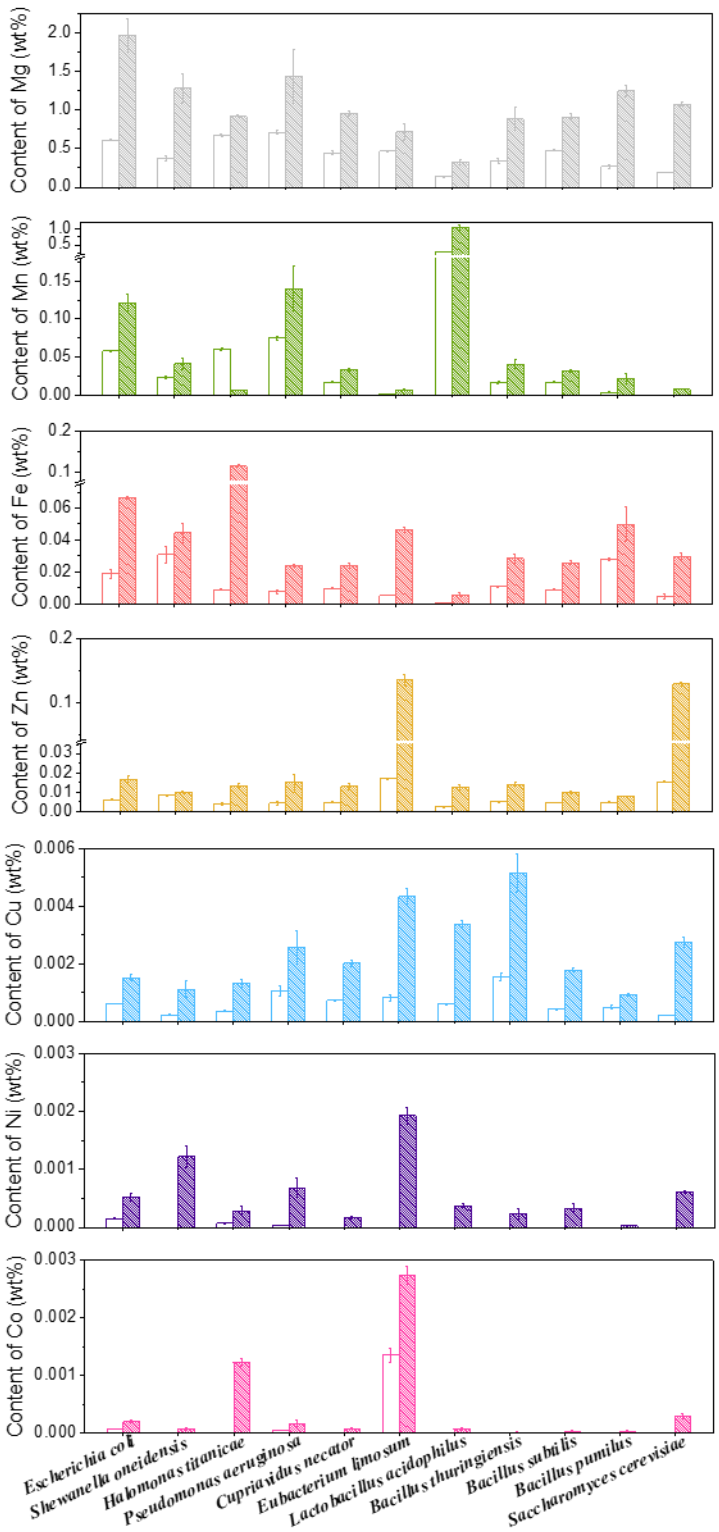

Supplementary Figure 3 | The content of the predominant metal elements in microorganisms (hollow) **and the corresponding derived carbon materials** (solid fill pattern) **measured by ICP-MS. a,** Mg, **b,** Mn, **c,** Fe, **d,** Zn, **e,** Cu, **f)** Ni, and **g,** Co. Error bars represent the standard deviation for three separate measurements.

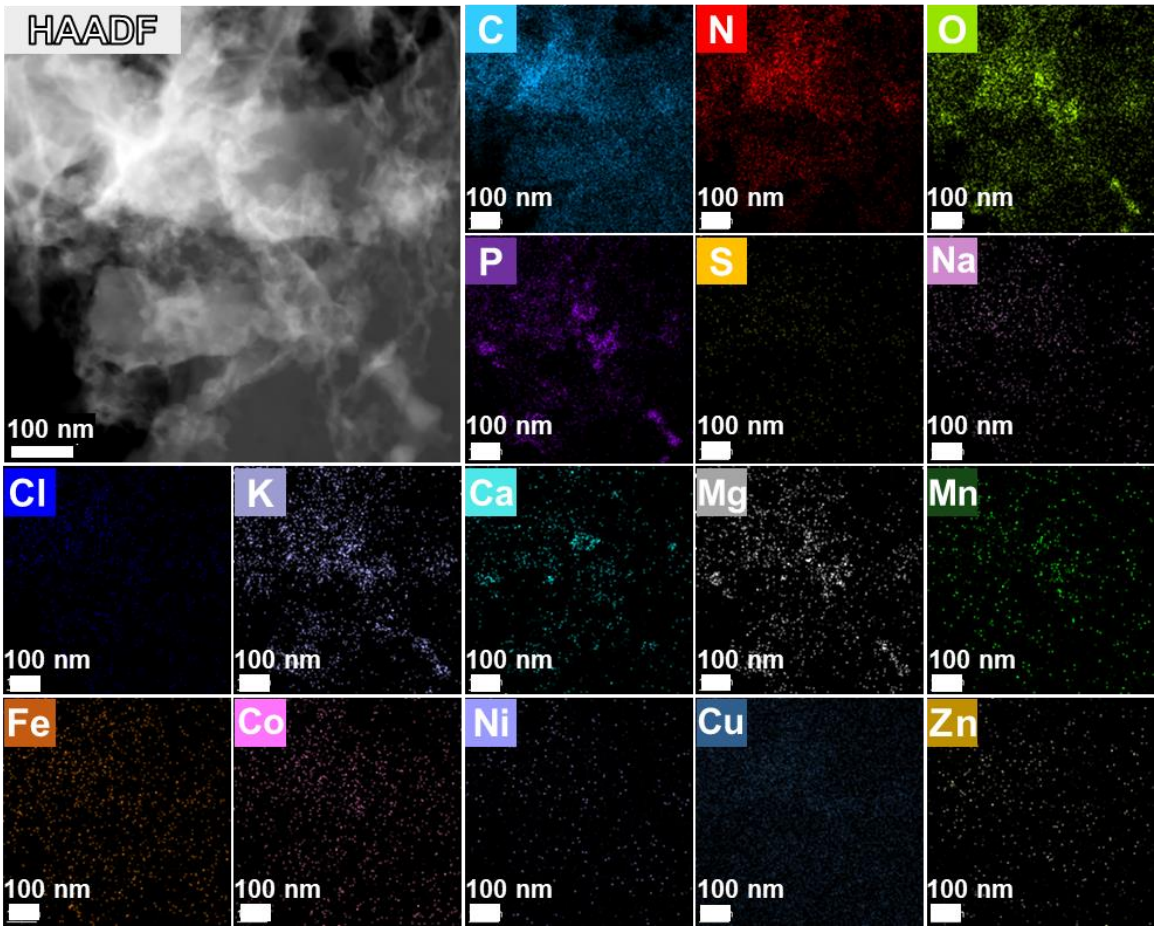

Supplementary Figure 4 | The STEM image and elemental distribution maps of *Escherichia coli*-derived carbon material.

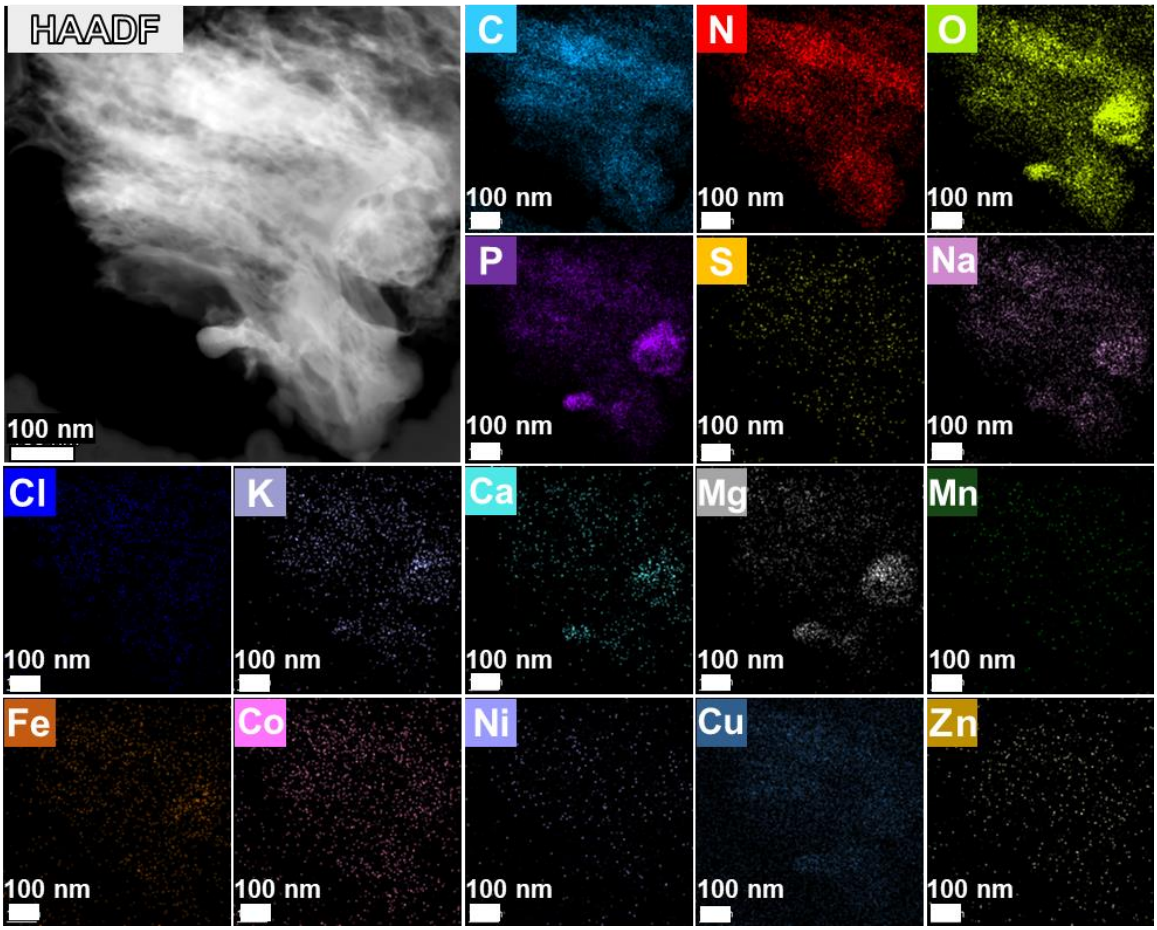

Supplementary Figure 5 | The STEM image and elemental distribution maps of *Shewanella oneidensis*-derived carbon material.

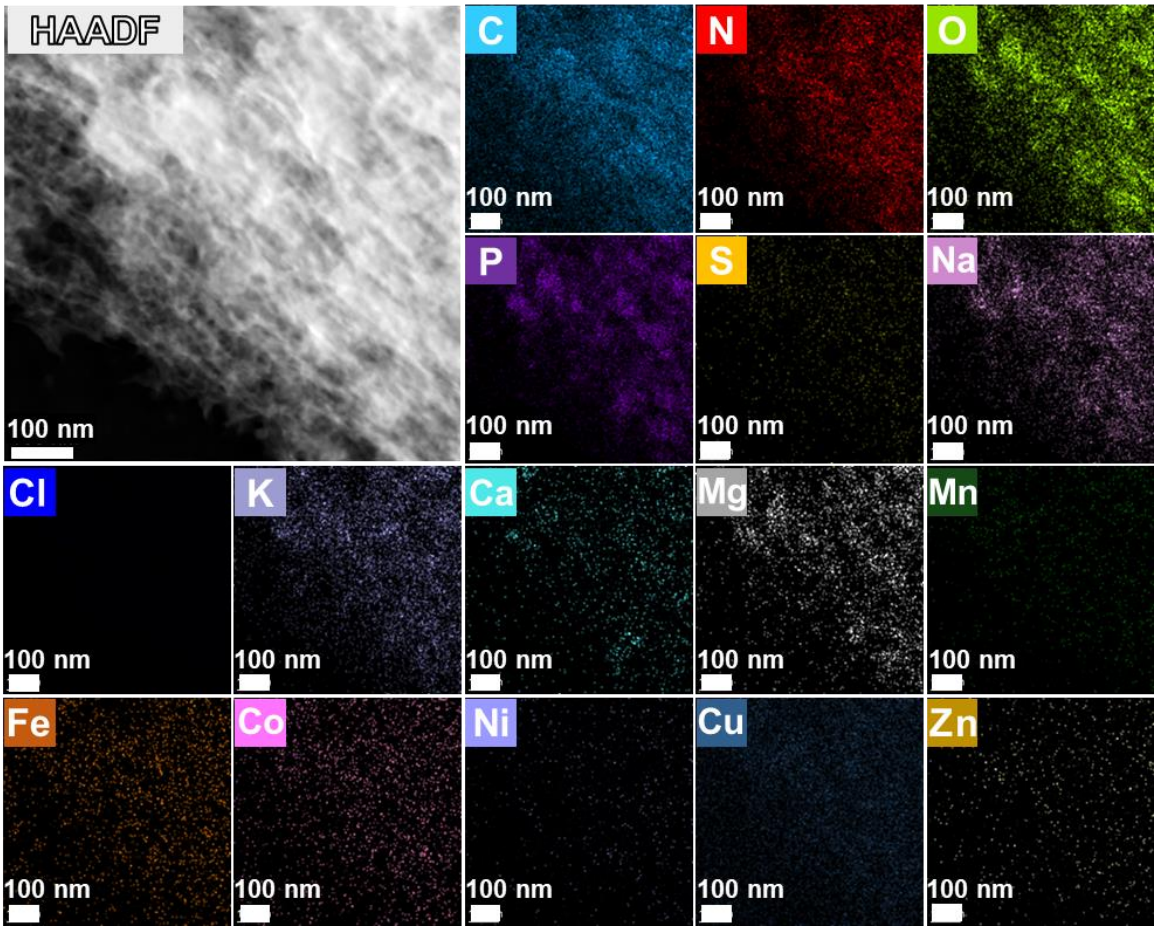

Supplementary Figure 6 | The STEM image and elemental distribution maps of *Halomonas titanicae*-derived carbon material.

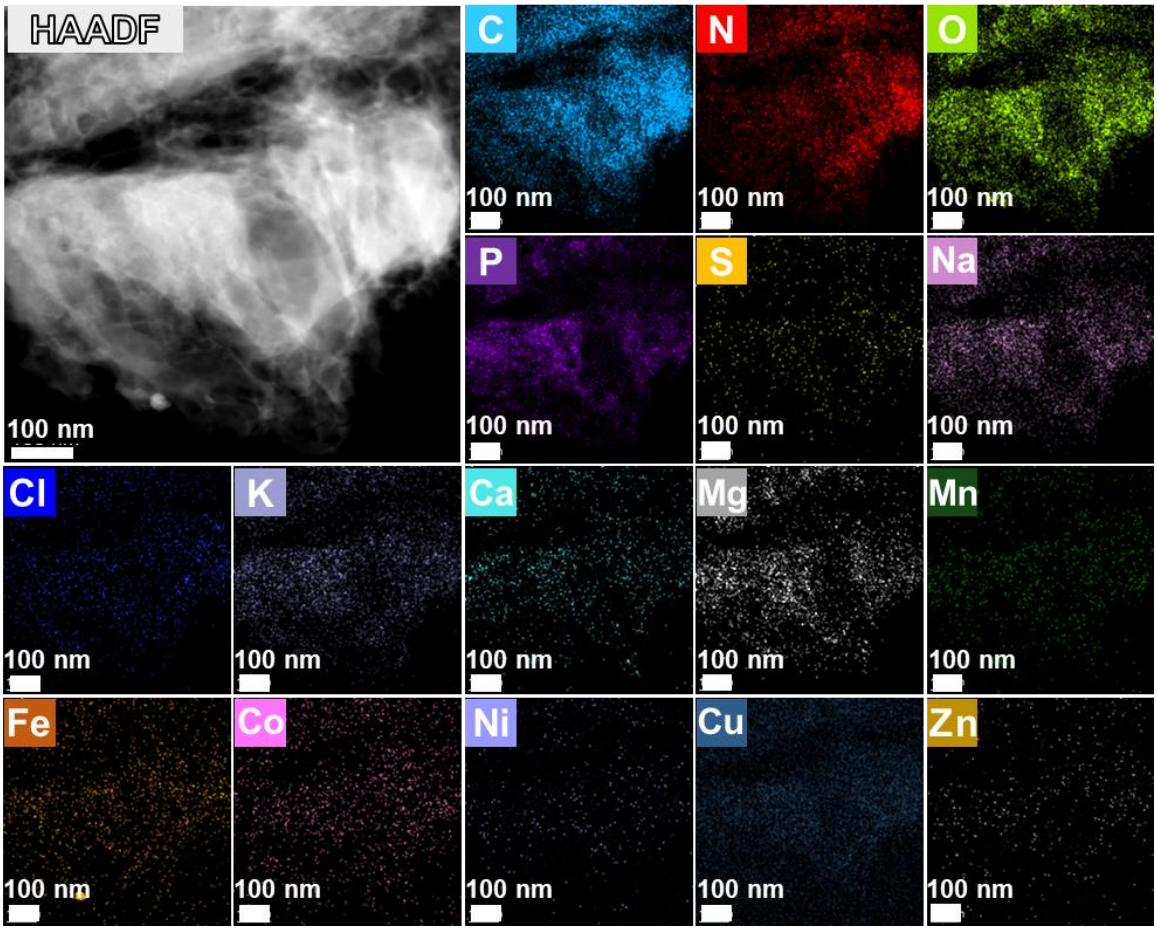

Supplementary Figure 7 | The STEM image and elemental distribution maps of *Pseudomonas aeruginosa*-derived carbon material.

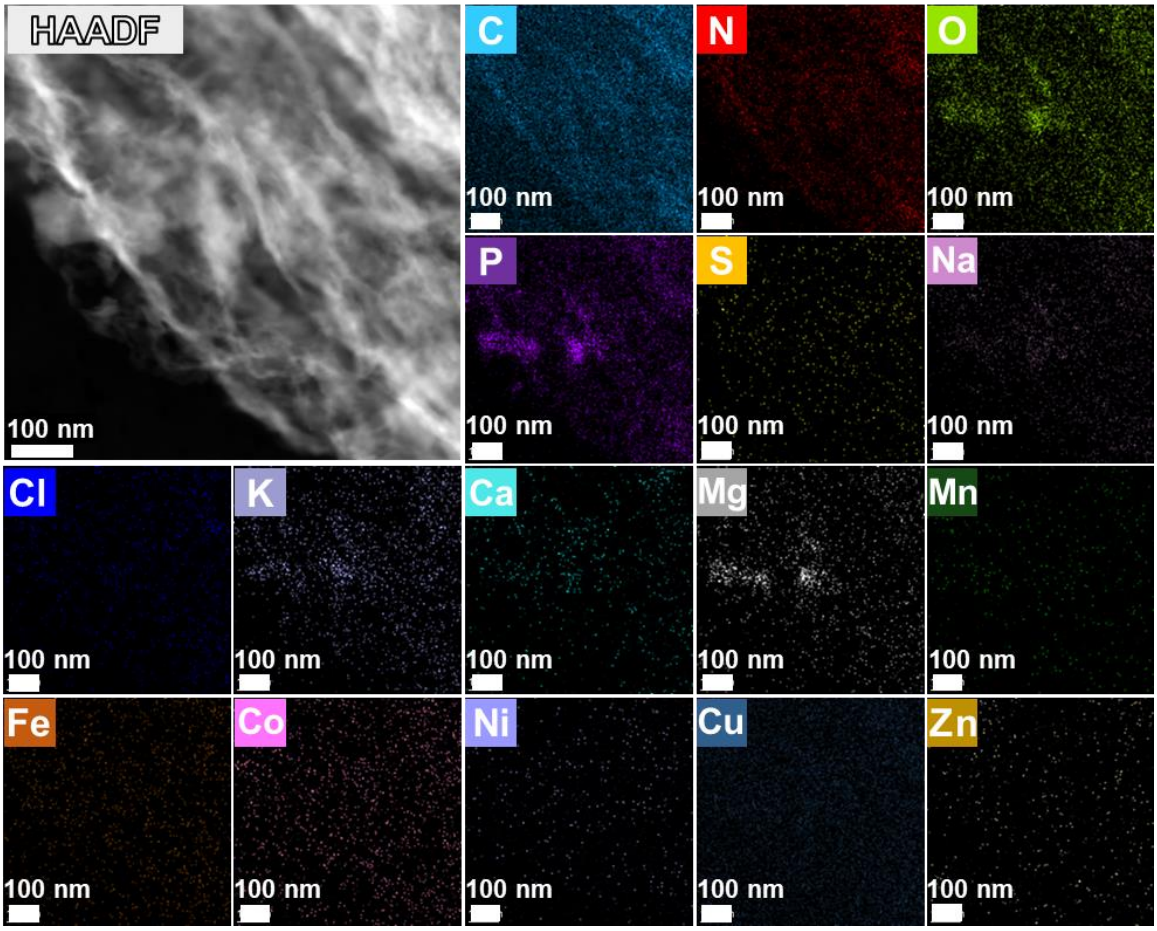

Supplementary Figure 8 | The STEM image and elemental distribution maps of *Cupriavidus necator*-derived carbon material.

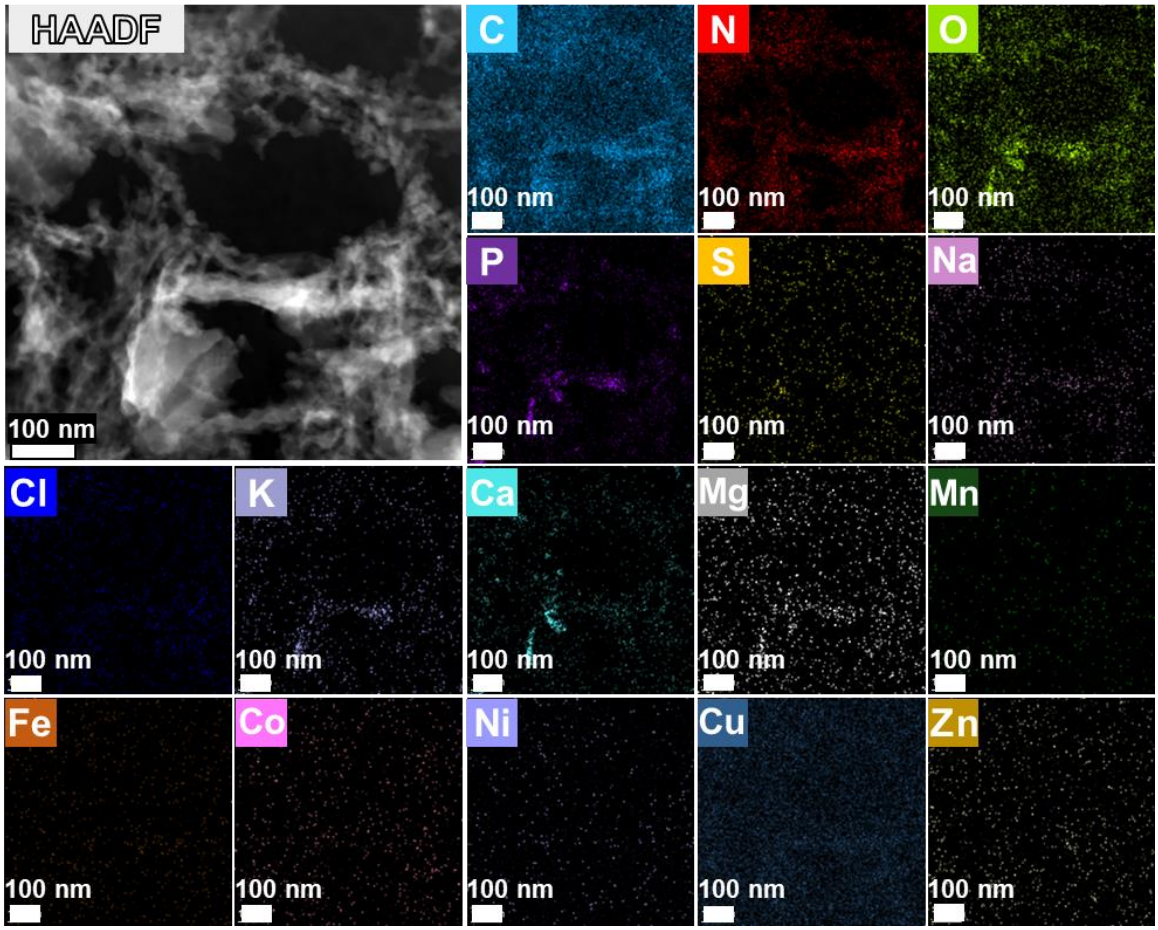

Supplementary Figure 9 | The STEM image and elemental distribution maps of *Eubacterium limosum*-derived carbon material.

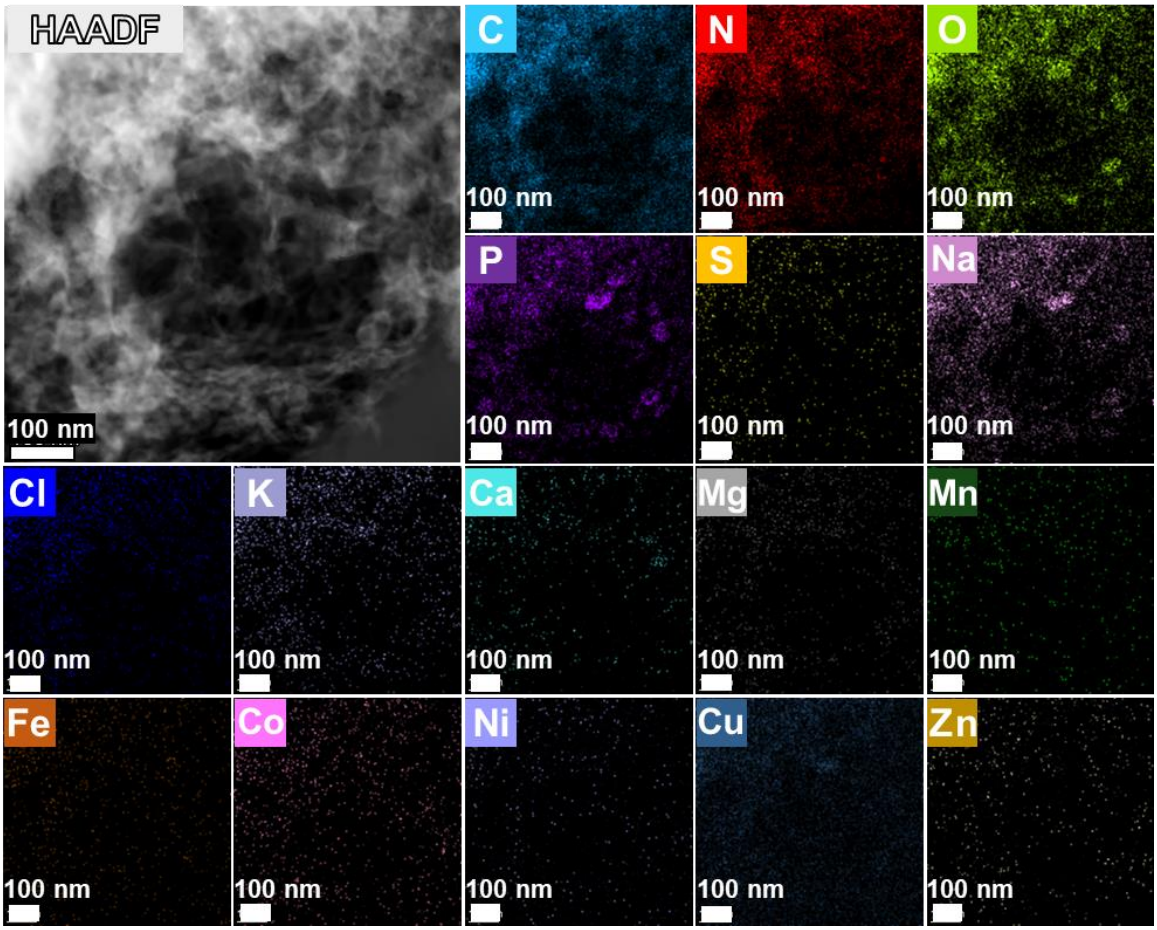

Supplementary Figure 10 | The STEM image and elemental distribution maps of *Lactobacillus acidophilus*-derived carbon material.

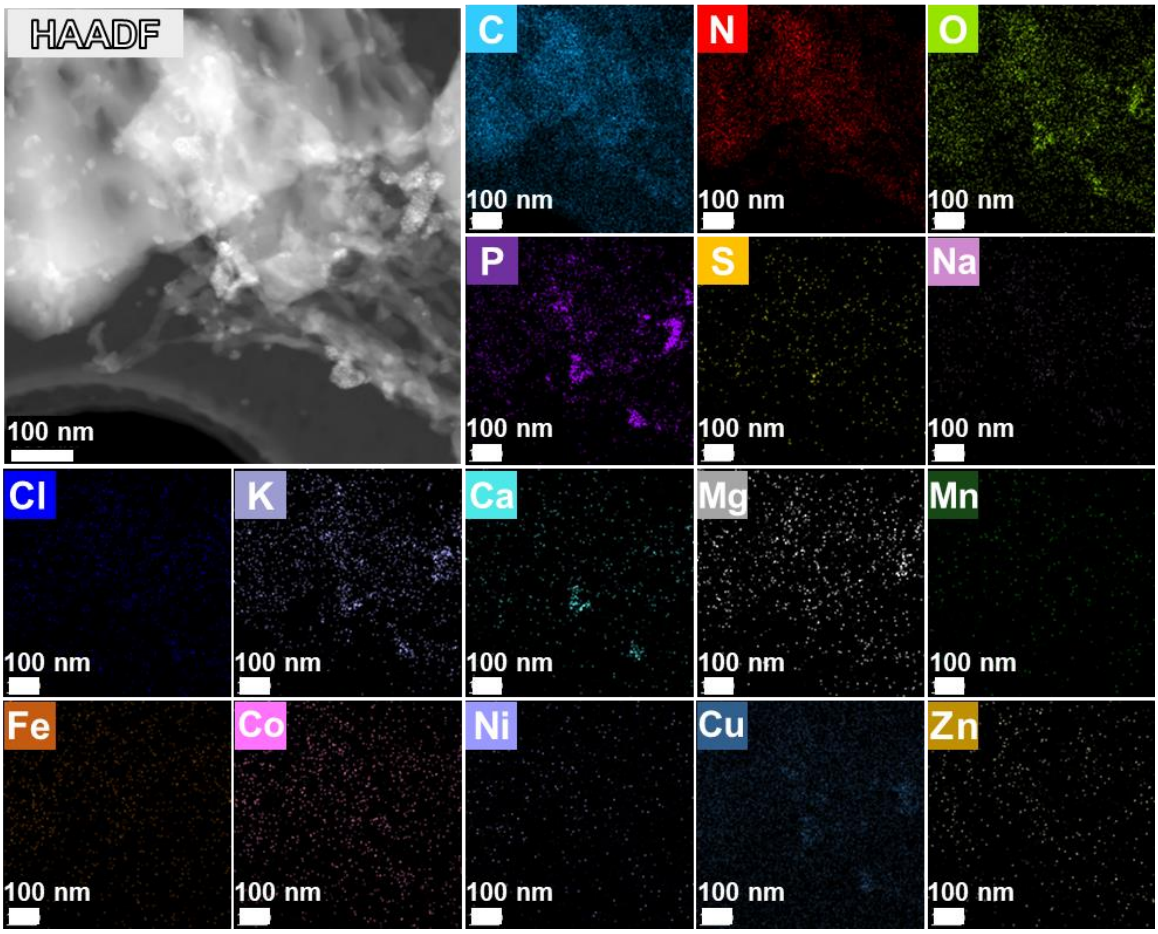

Supplementary Figure 11 | The STEM image and elemental distribution maps of *Bacillus thuringiensis*-derived carbon material.

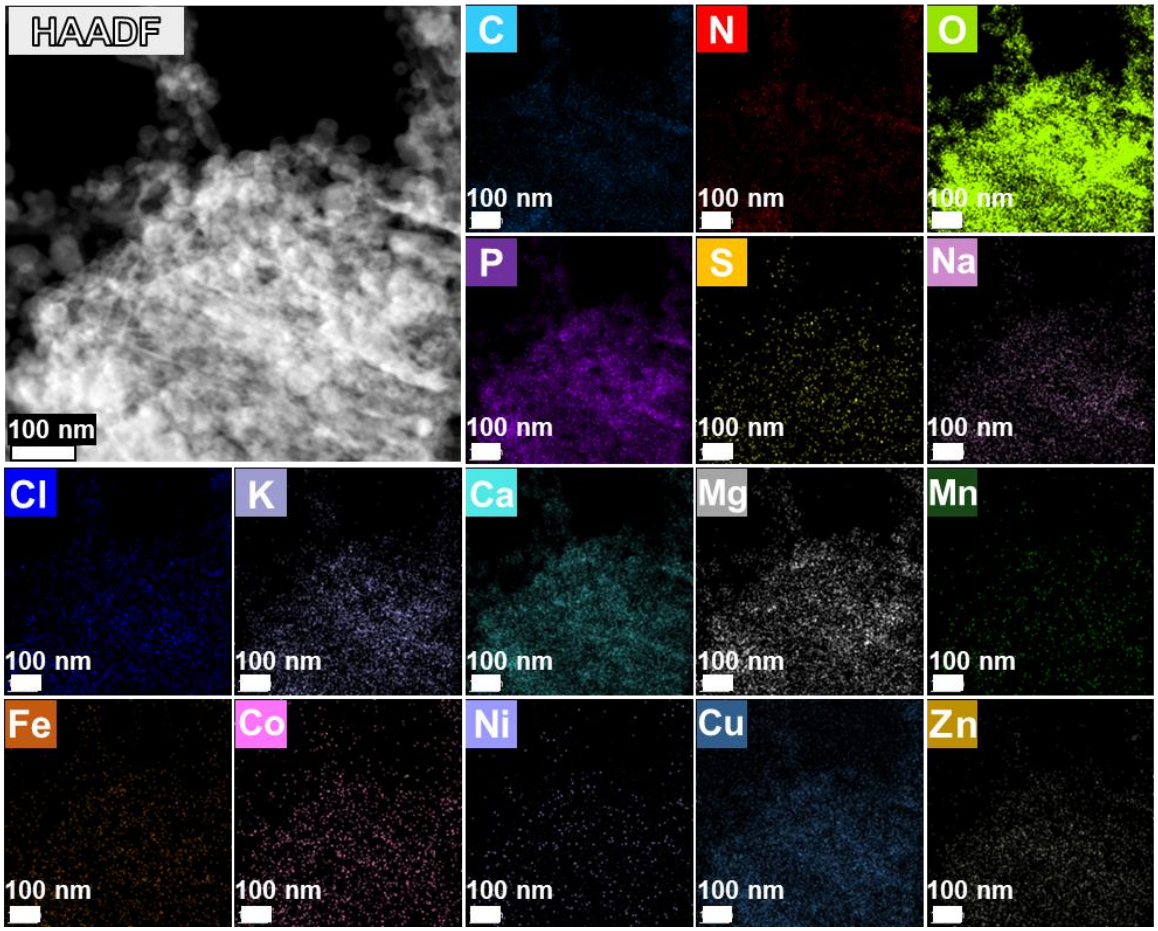

Supplementary Figure 12 | The STEM image and elemental distribution maps of *Bacillus subtilis*-derived carbon material.

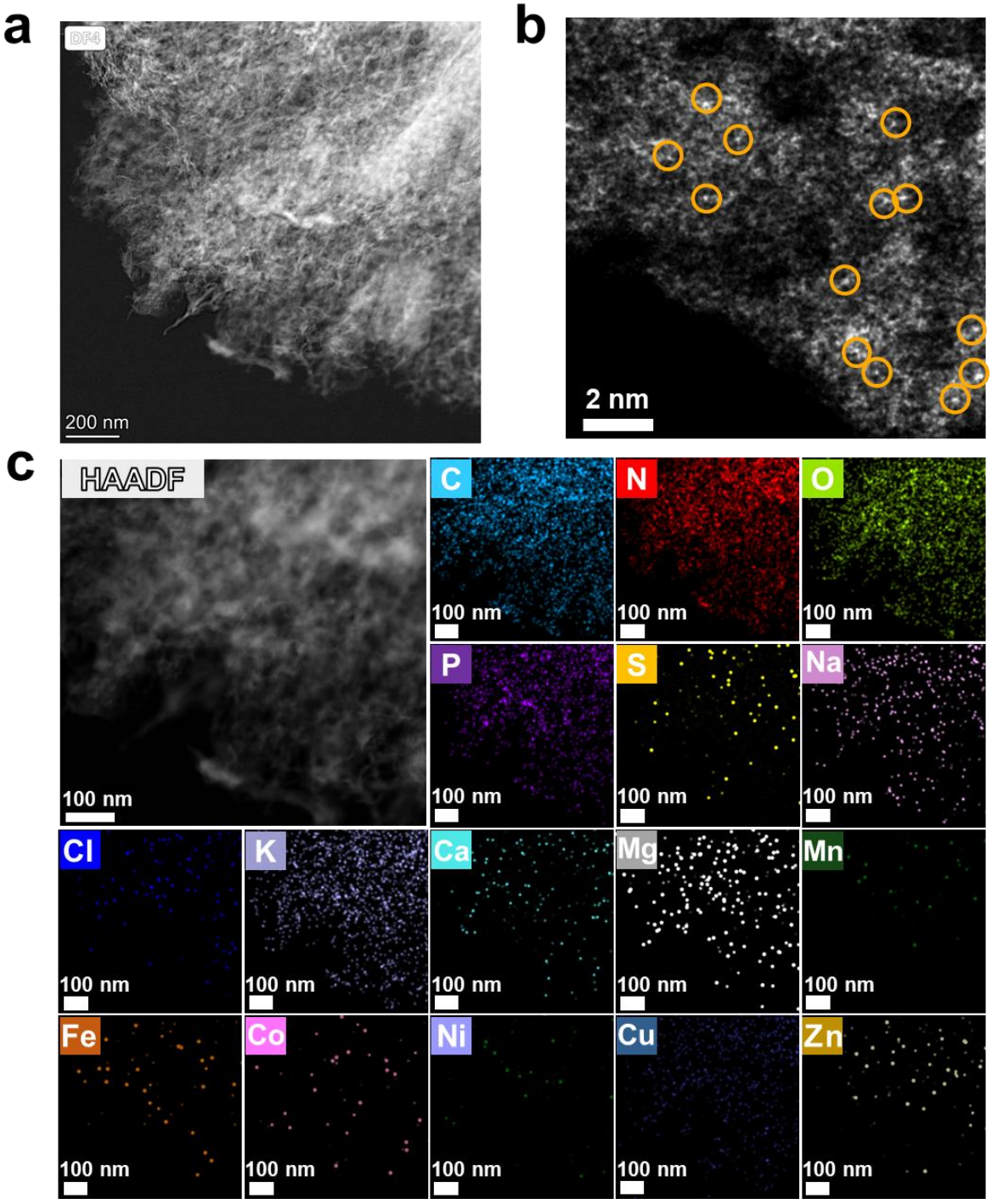

Supplementary Figure 13 | The AC-STEM images and elemental distribution maps of *Bacillus pumilus*-derived carbon material. a, Dark field image, **b,** High resolution HAADF-STEM image and **c,** Elemental distribution map. Metal atoms are monodisperse as marked with yellow circles in high resolution HAADF-STEM image.

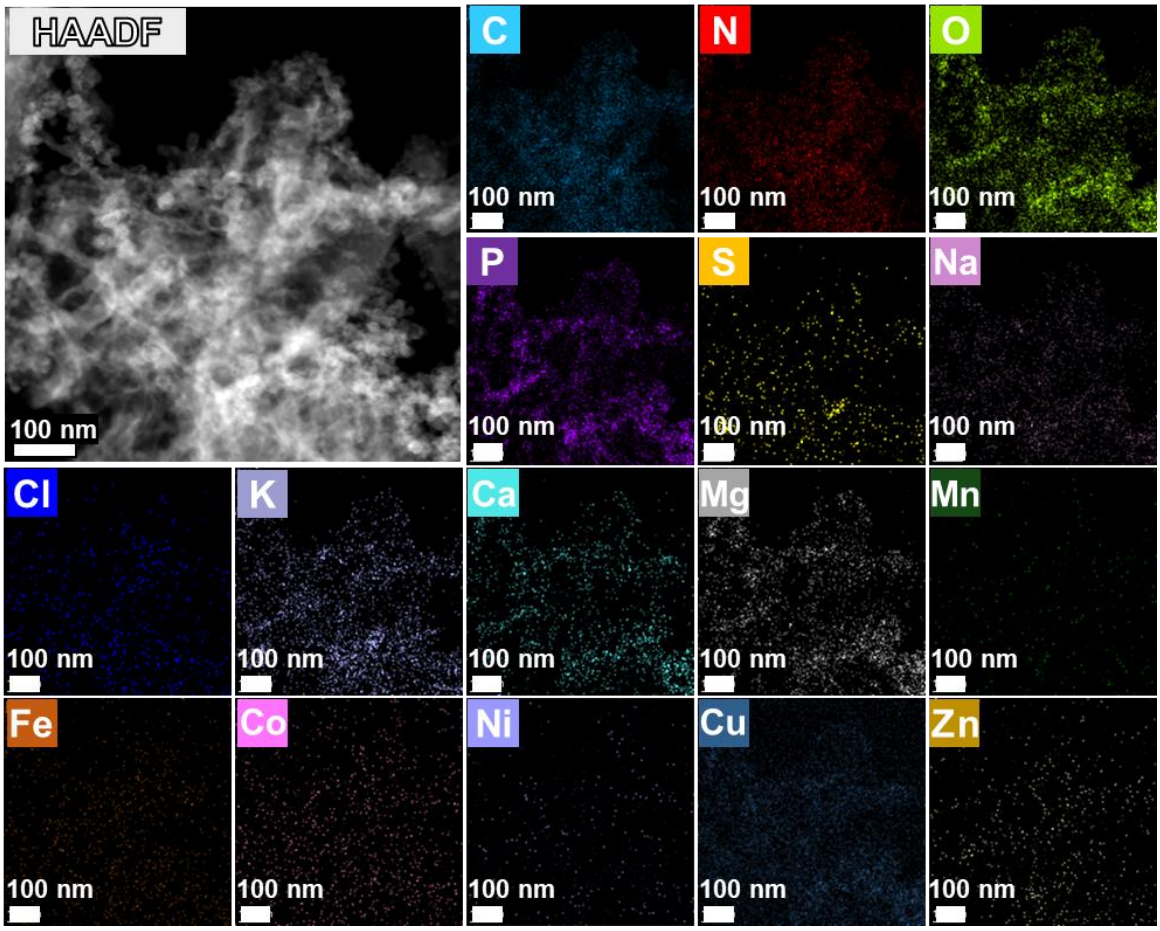

Supplementary Figure 14 | The STEM image and elemental distribution maps of *Saccharomyces cerevisiae*-derived carbon material.

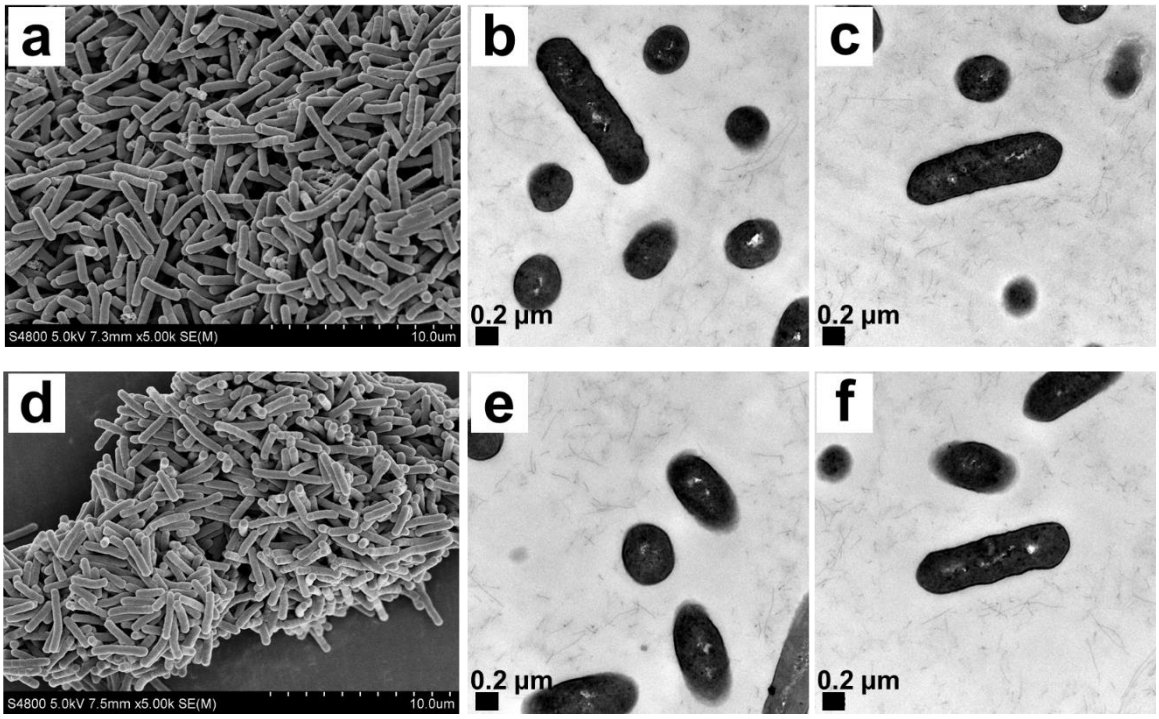

Supplementary Figure 15 | The morphology of *Bacillus pumilus* and *Bacillus pumilus*(Fe−). *Bacillus pumilus* is often used as an industrial fermentative bacterium, being easy to culture with a short growth period. *Bacillus pumilus* will express a variety of iron-containing structures, for example, Siderophores, Fe-superoxide dismutase, Heme-containing enzymes/proteins. **a,** SEM images of vegetative *Bacillus pumilus* cells. **b-c**, TEM images of the biology slice taken from biopsy samples of osmium acid and lead acetate pre-treated *Bacillus pumilus*. **d**, SEM images of vegetative *Bacillus pumilus*(Fe−) cells. **e-f**, TEM images of the biology slice taken from biopsy samples of osmium acid and lead acetate pre-treated *Bacillus pumilus*(Fe−) cells.

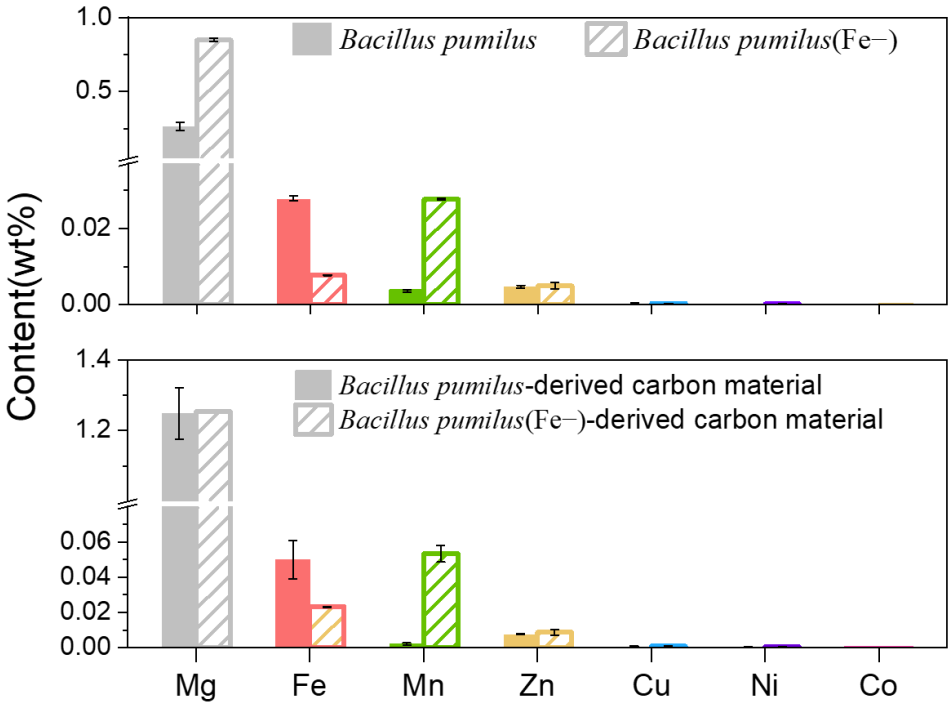

Supplementary Figure 16 | The content of metal elements in *Bacillus pumilus*, *Bacillus pumilus*(Fe−), *Bacillus pumilus*-derived carbon material and *Bacillus pumilus*(Fe−)-derived carbon material. Error bars represent the standard deviation for three separate measurements.

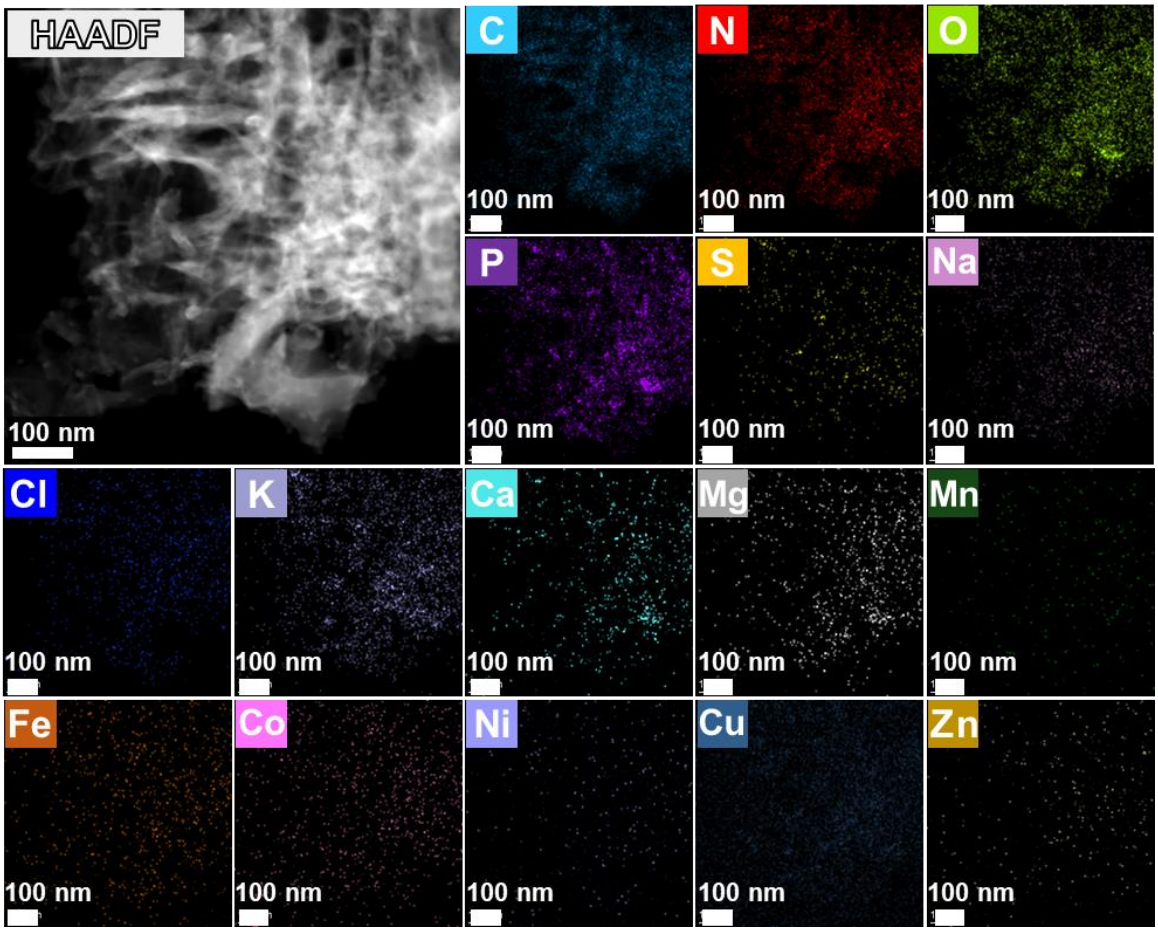

Supplementary Figure 17 | The STEM and elemental distribution map of *Bacillus pumilus*(Fe−)-derived carbon material.

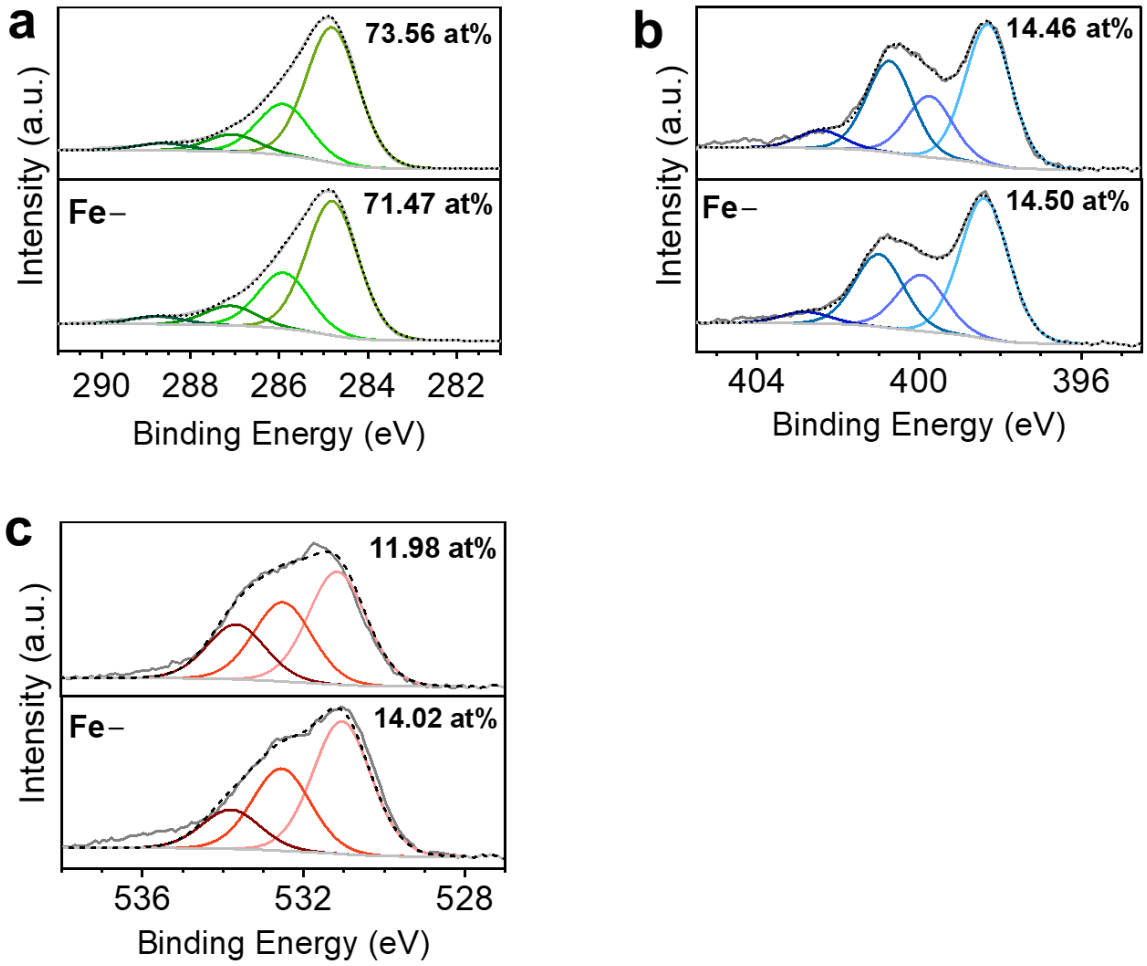

Supplementary Figure 18 | XPS spectra of *Bacillus pumilus*-derived carbon material (top) **and *Bacillus pumilus*(Fe−)-derived carbon material** (down)**. a,** C 1s spectra, **b,** N 1s spectra, and **c,** O 1s spectra.

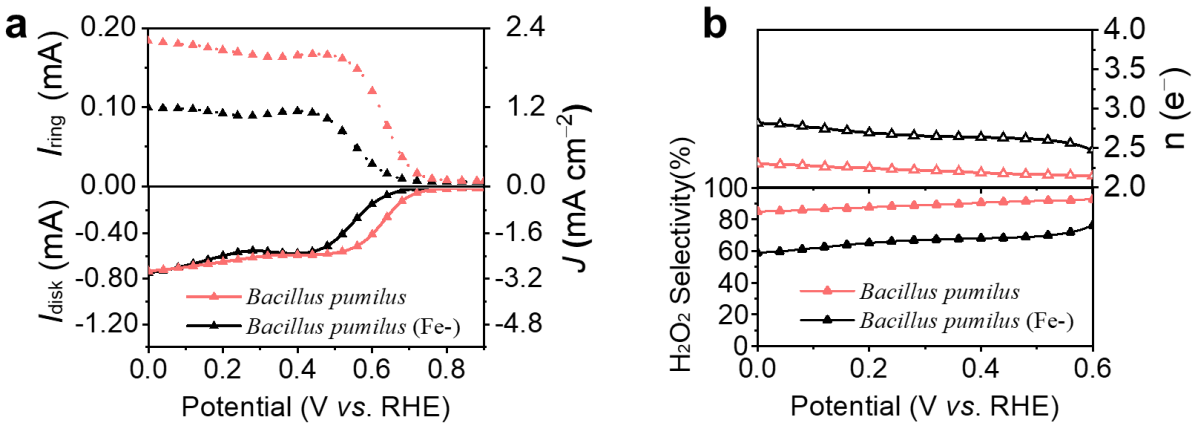

Supplementary Figure 19 | ORR electrochemical performance of *Bacillus pumilus*-derived carbon material and *Bacillus pumilus*(Fe−)-derived carbon material. a, ORR polarization curve. **b**, Calculated ORR electron transfer number and H_2O_2 selectivity.

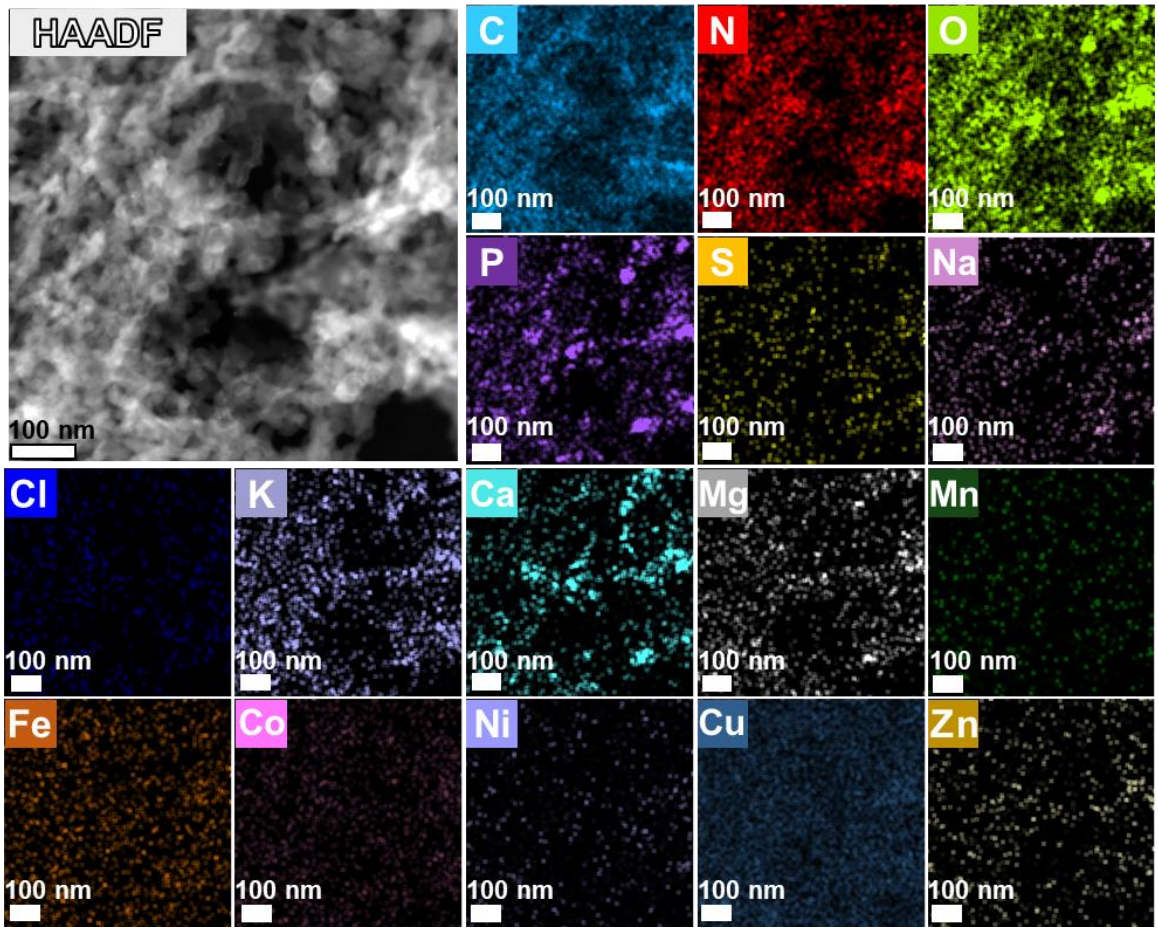

Supplementary Figure 20 | The STEM image and elemental distribution maps of *Bacillus pumilus*-derived carbon material obtained at 450°C.

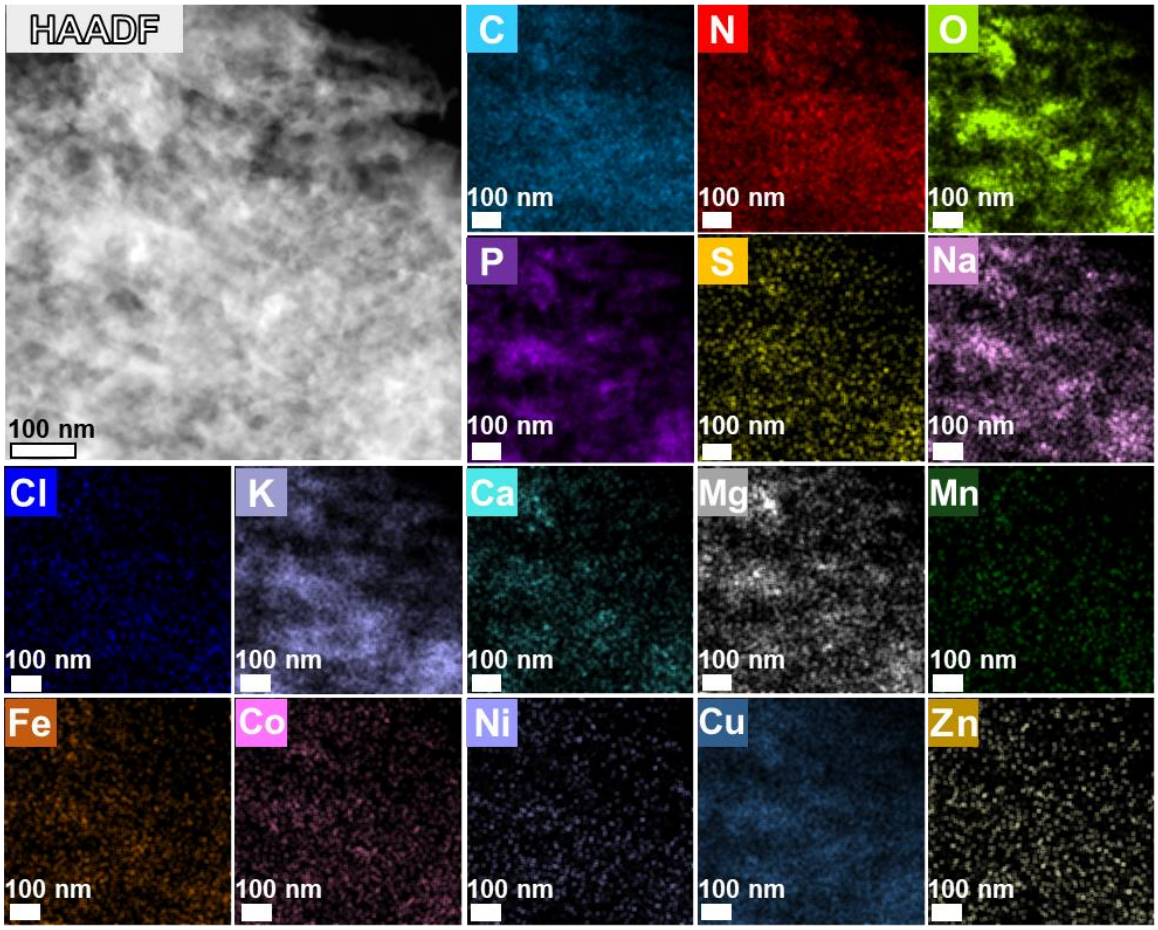

Supplementary Figure 21 | The STEM image and elemental distribution maps of *Bacillus pumilus*-derived carbon material obtained at 500°C.

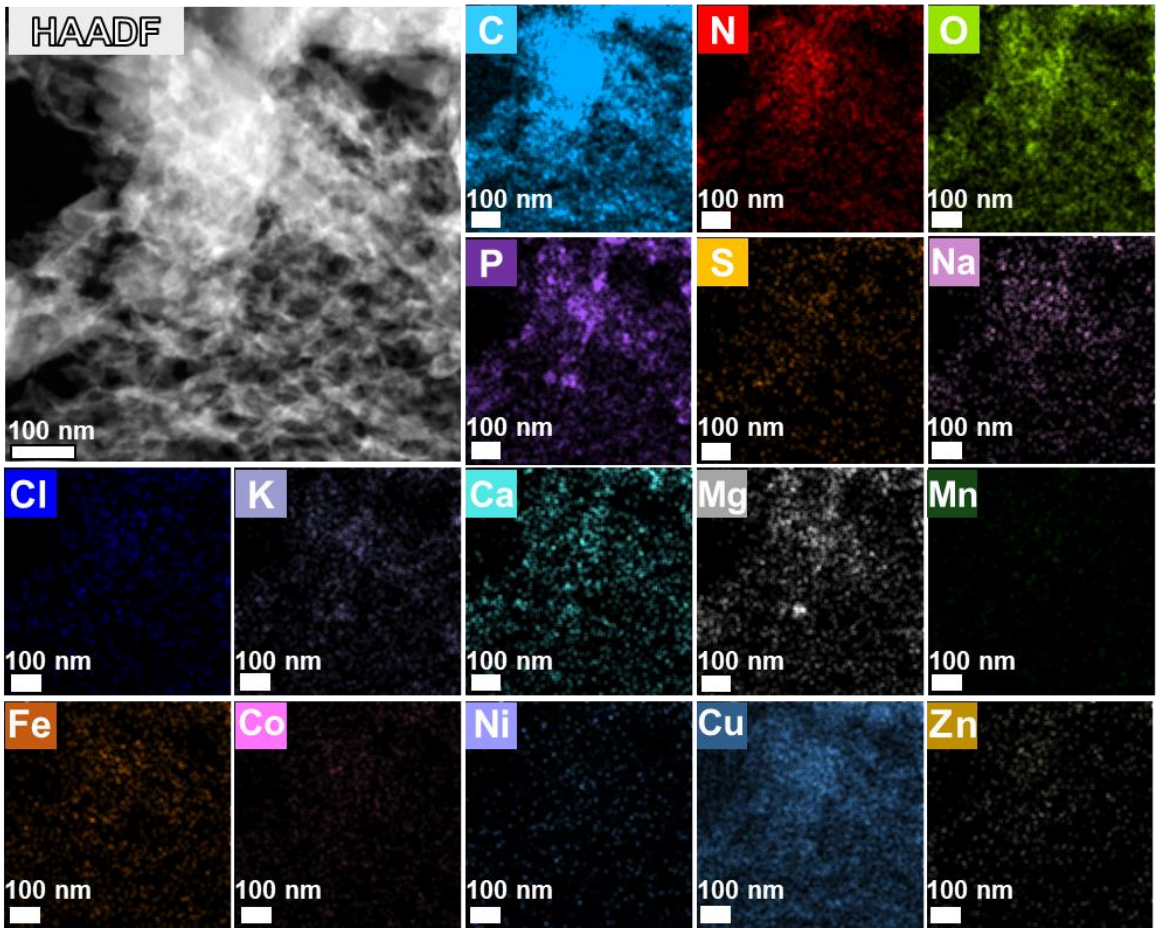

Supplementary Figure 22 | The STEM image and elemental distribution maps of *Bacillus pumilus*-derived carbon material obtained at 700°C.

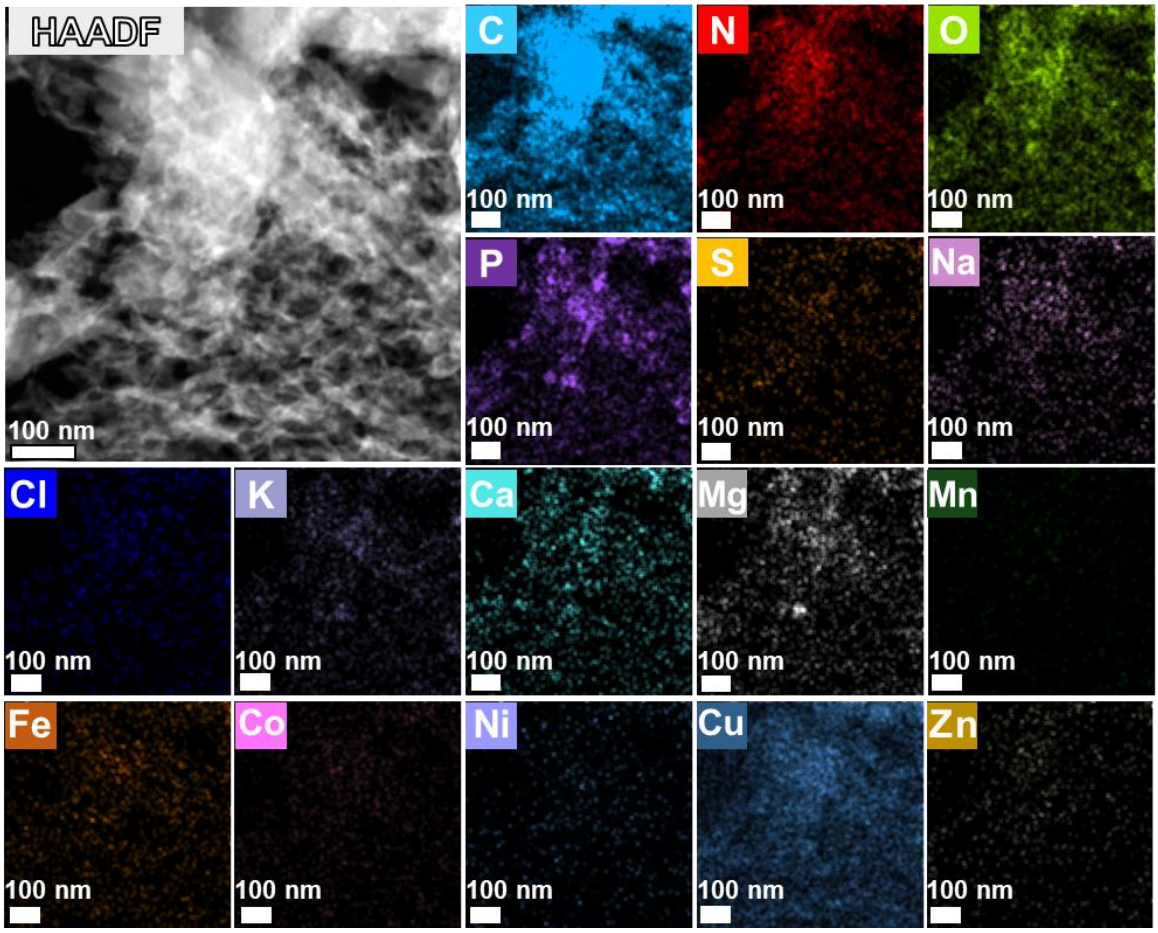

Supplementary Figure 23 | The STEM image and elemental distribution maps of *Bacillus pumilus*-derived carbon material obtained at 900°C.

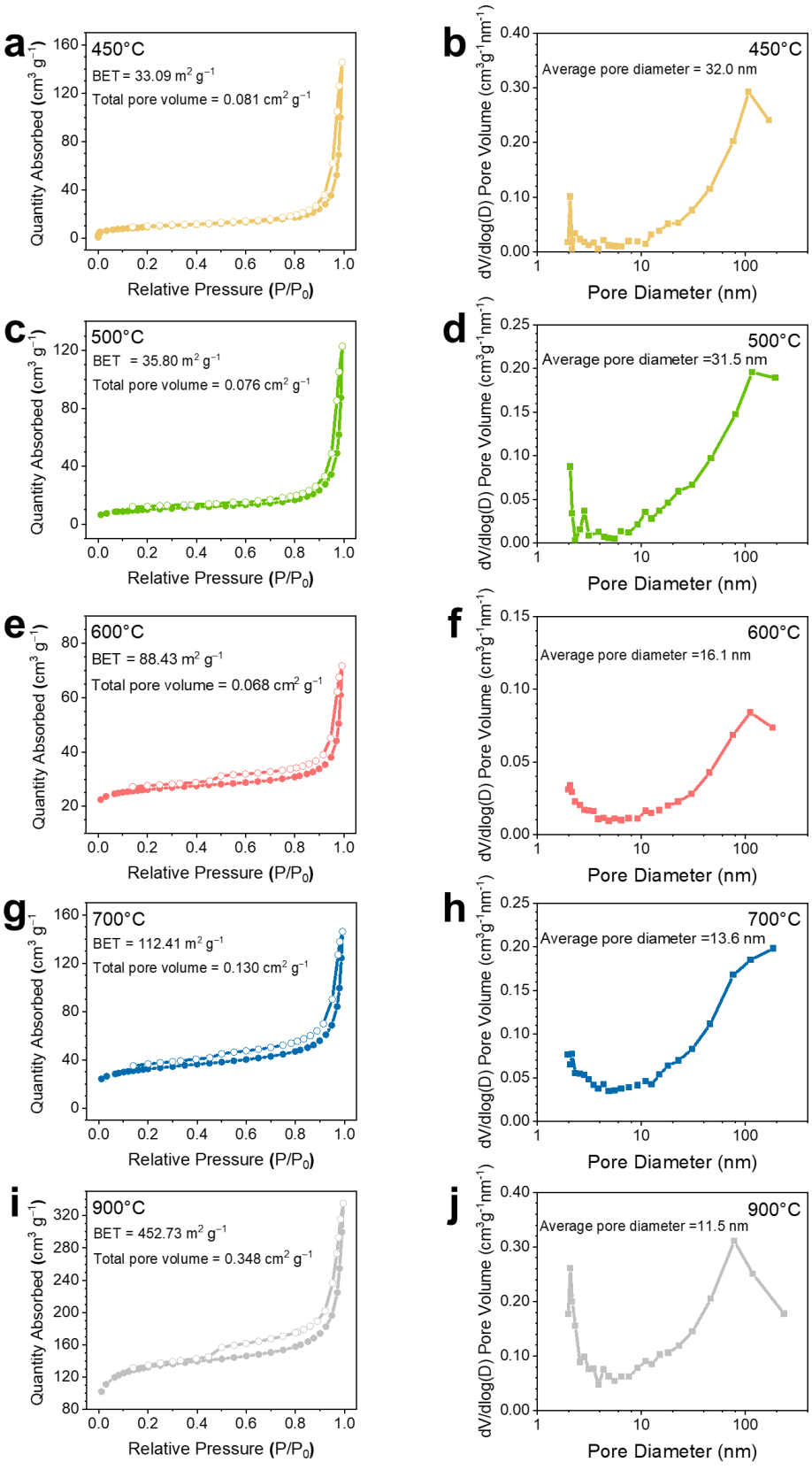

Supplementary Figure 24 | The specific surface and pore distribution of *Bacillus pumilus*-derived carbon materials obtained at different temperatures. **a**, **c**, **e**, **g**, and **i**, Nitrogen adsorption-desorption isotherms (labeled as solid and hollow) and **b**, **d**, **f**, **h**, and **j**, the corresponding pore size distribution.

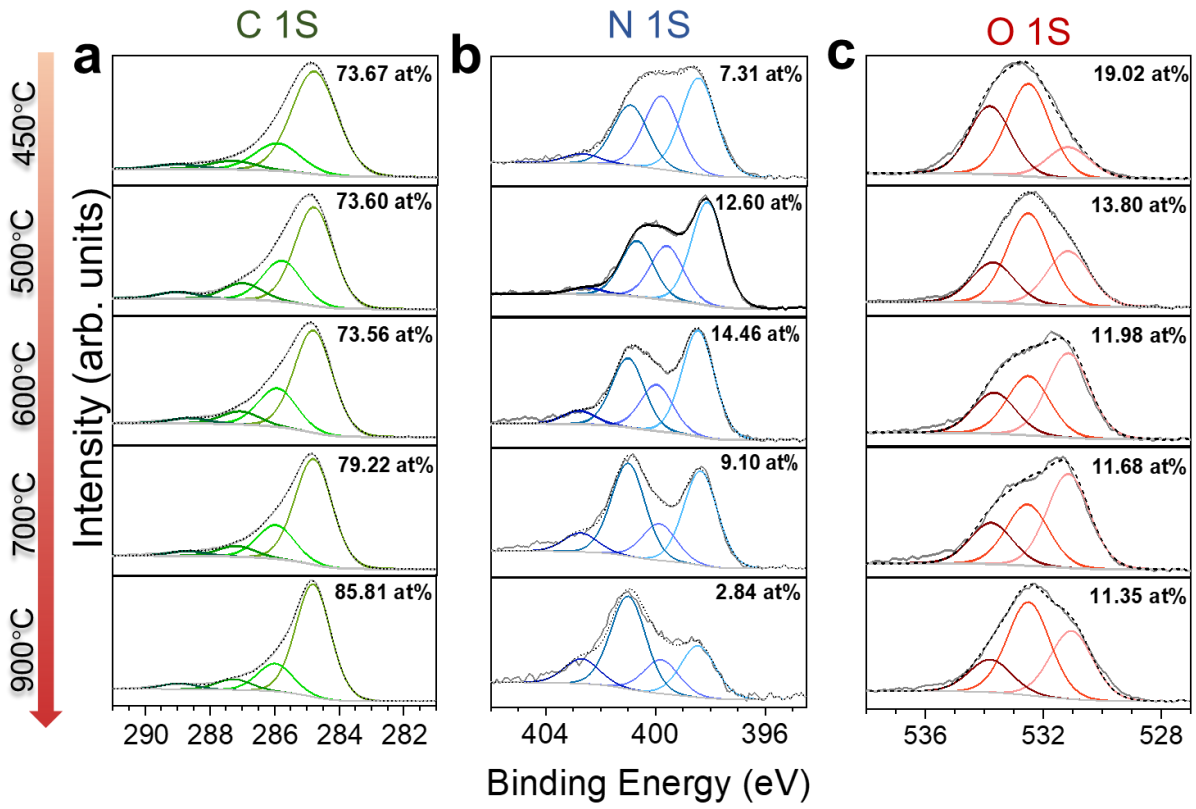

Supplementary Figure 25 | XPS spectra of *Bacillus pumilus*-derived carbon materials obtained at different tempretures. a, C 1s spectra, **b,** N 1s spectra, and **c,** O 1s spectra.

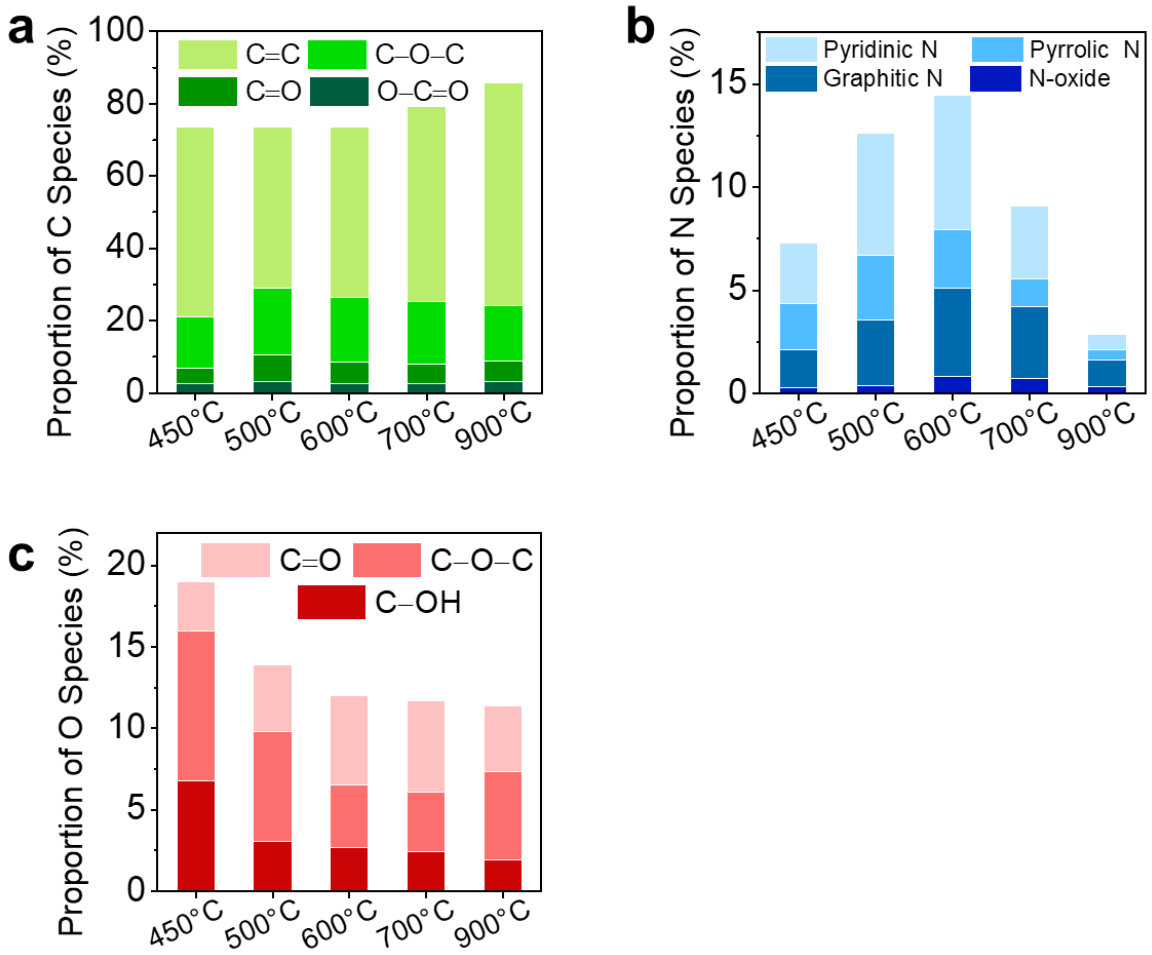

Supplementary Figure 26 | Fraction analysis from XPS spectra of *Bacillus pumilus*-derived carbon materials obtained at different tempretures. a, C fraction**, b,** N fraction and **c,** O fraction.

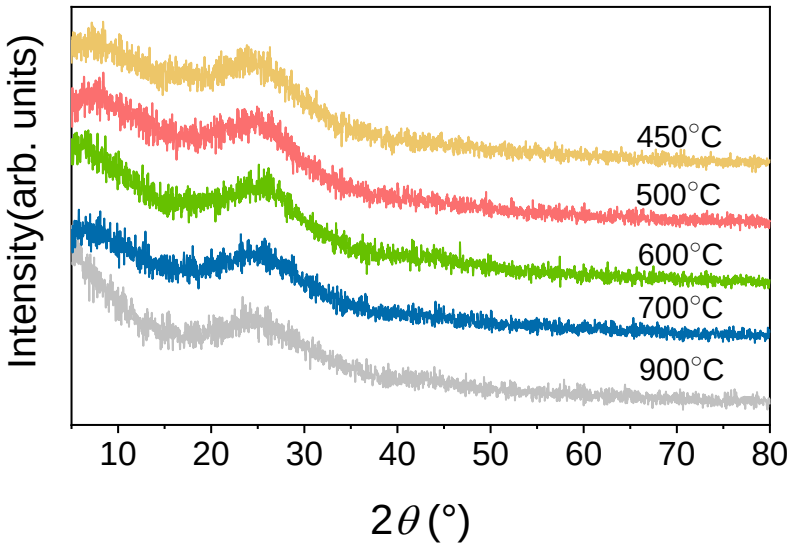

Supplementary Figure 27 | XRD patterns of *Bacillus pumilus*-derived carbon materials obtained at different tempretures.

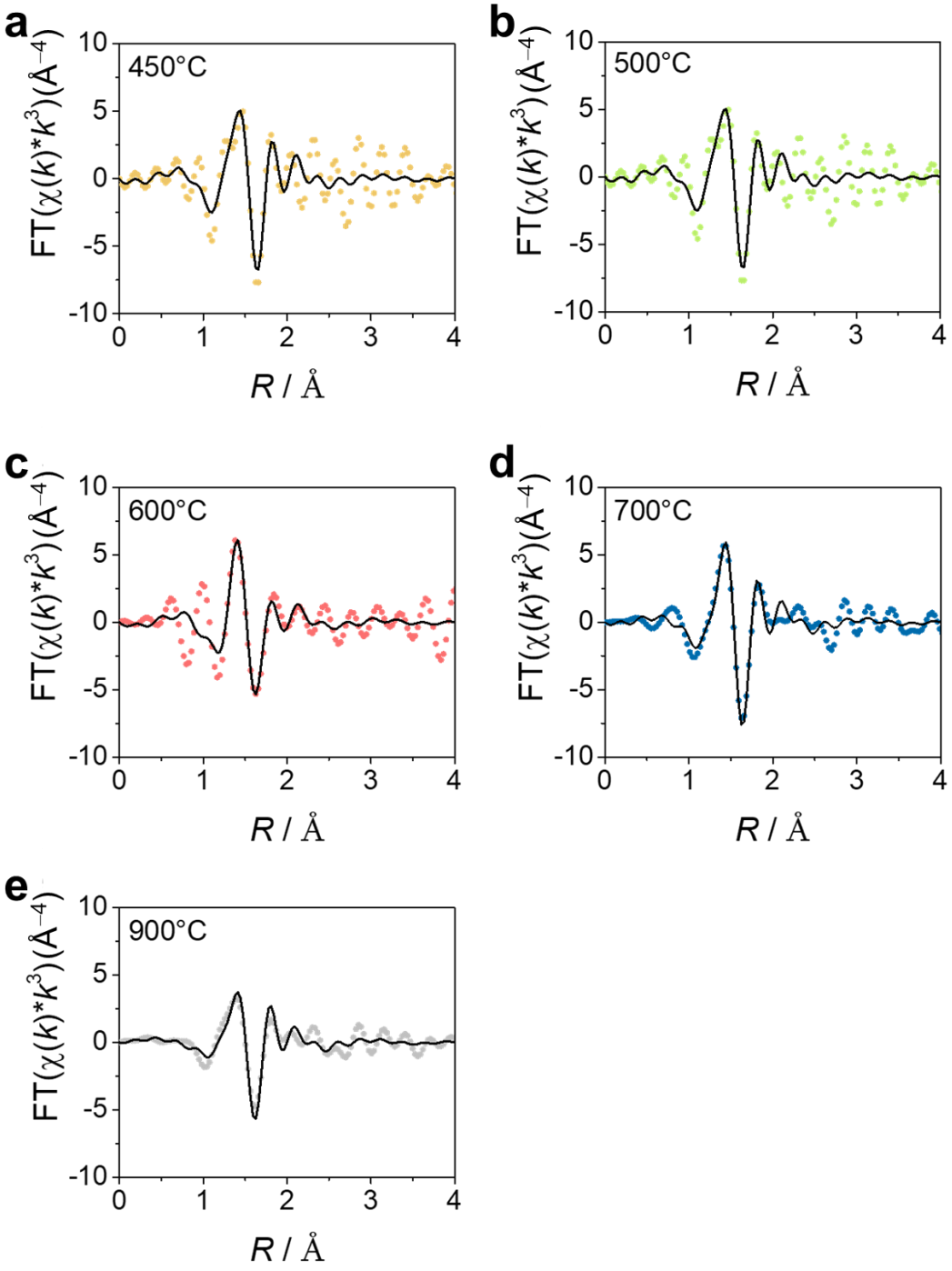

Supplementary Figure 28 | Fe K-edge EXAFS (point) and the curve fit (line) for $FeN_{5-x}O_x$ and FeN_4 catalysts, shown in k^3-weighted *k*-space after Fourier transform (Fourier transform magnitude component).

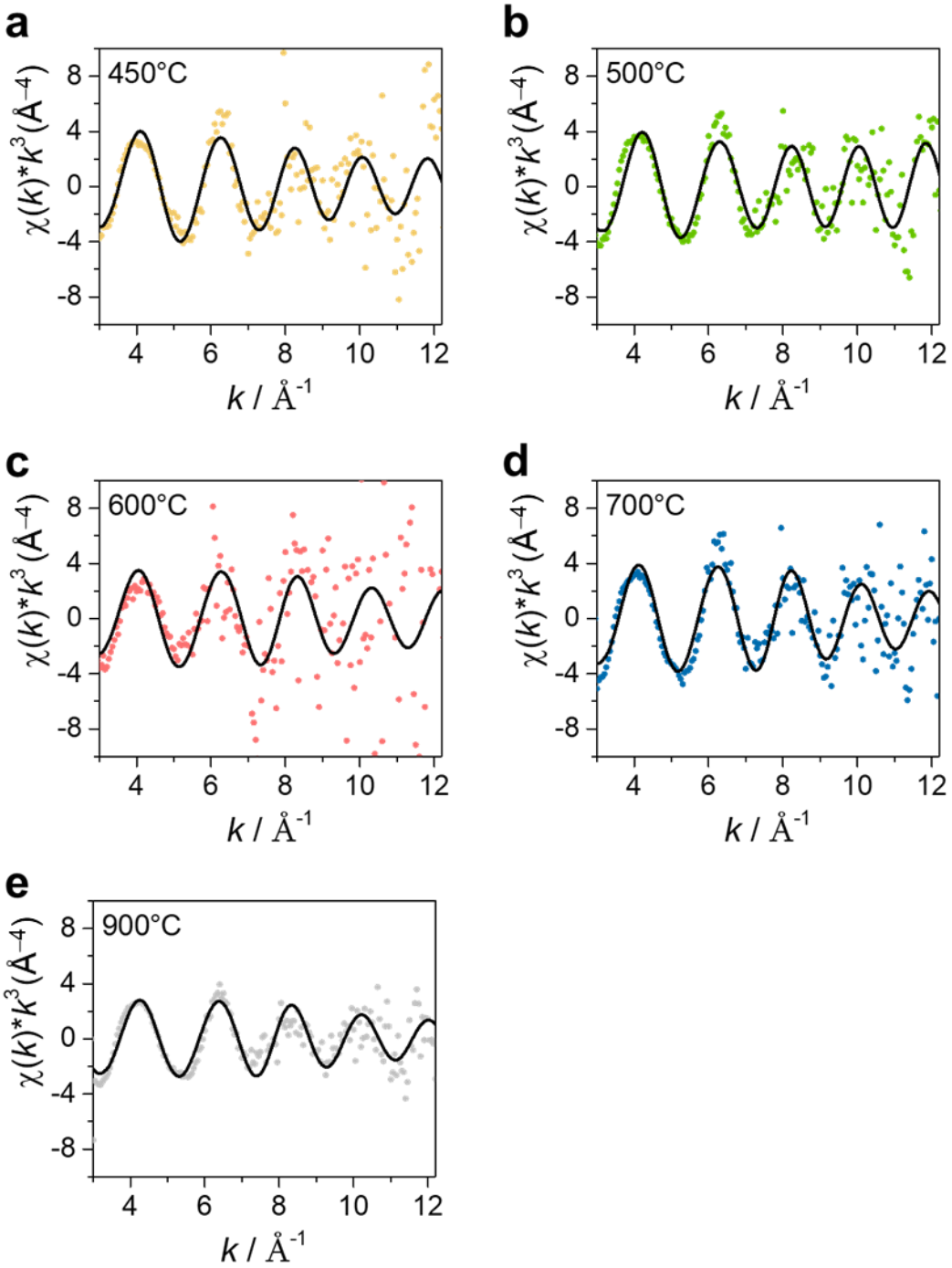

Supplementary Figure 29 | Fe K-edge EXAFS (point) and the curve fit (line) for $FeN_{5-x}O_x$ and FeN_4 catalysts, shown in k^3-weighted *k*-space after Fourier transform (Fourier transform imaginary component).

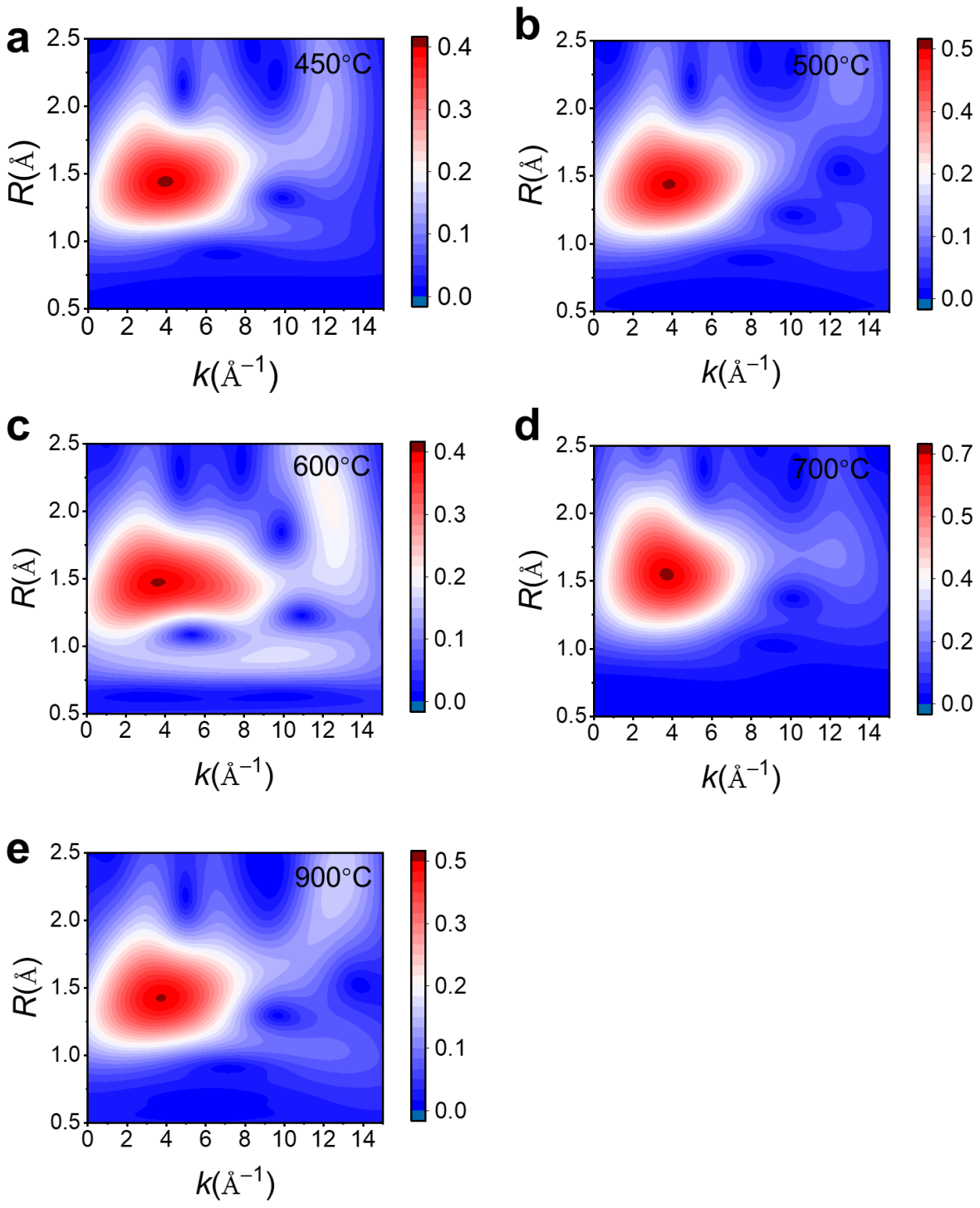

Supplementary Figure 30 | Wavelet transform for the k²-weighted Fe K-edge EXAFS signals of $FeN_{5-x}O_x$ and FeN_4 catalysts.

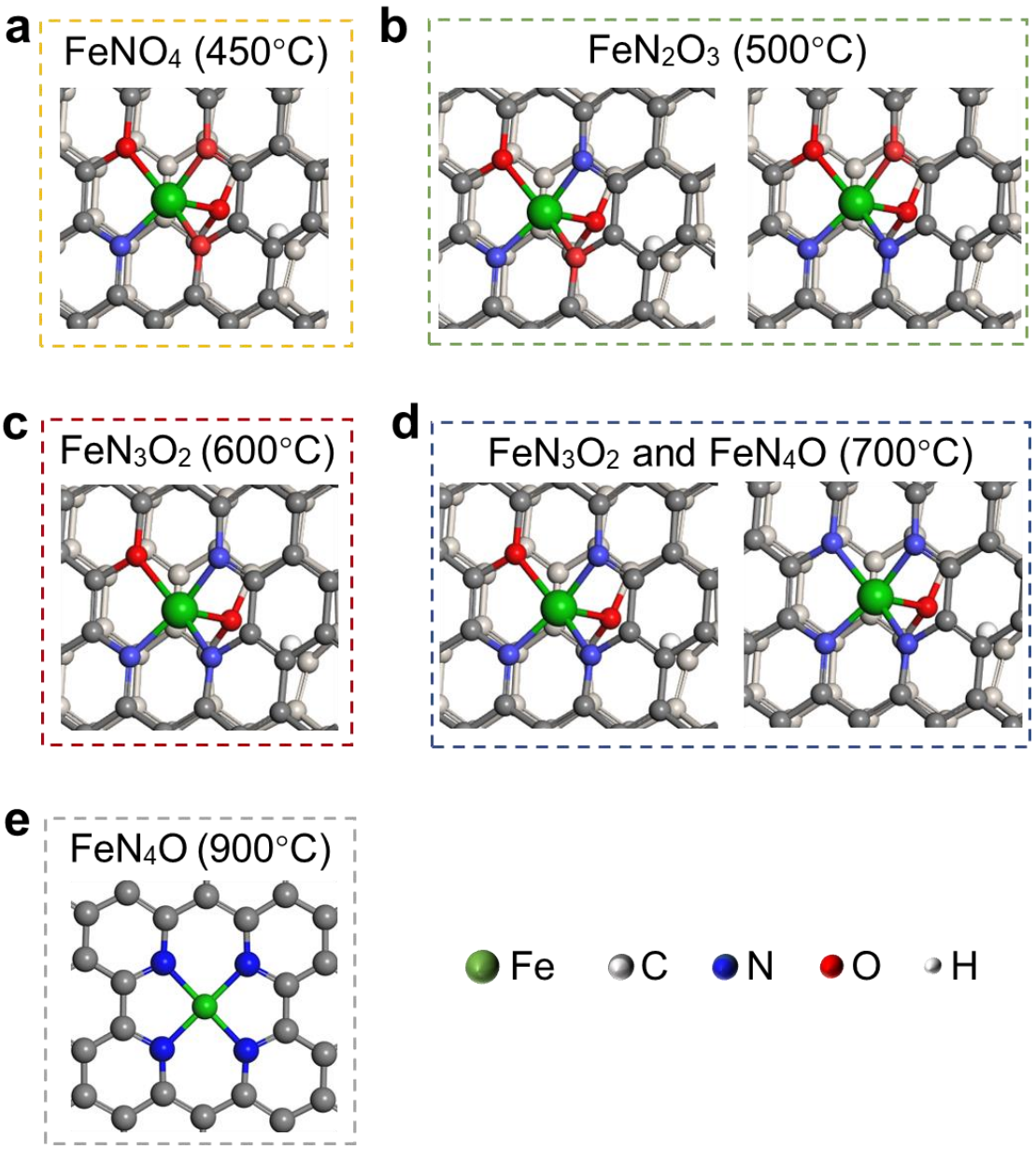

Supplementary Figure 31 | Schematic of proposed $FeN_{5-x}O_x$ and FeN_4 sites. a, $FeNO_4$, **b,** FeN_2O_3, **c,** FeN_3O_2, **d,** FeN_4O, and **e,** FeN_4.

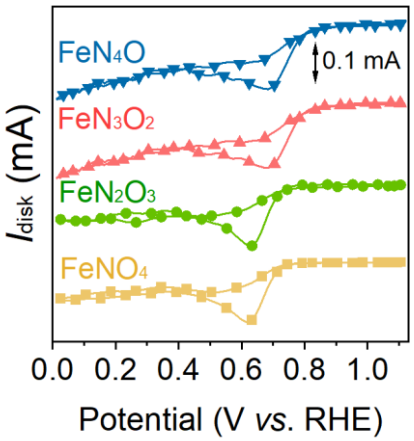

Supplementary Figure 32 | ORR intrinsic activity of $FeN_{5-x}O_x$ catalysts. The ORR peak of $FeN_{5-x}O_x$ catalysts was observed in the cyclic voltammetry in O_2-saturated 0.1 M KOH at 0 rpm. And the cyclic voltammetry curves were record at a scan rate of 50 mV s^{-1}. The measurements data were corrected for the double layer current using nitrogen saturation background.

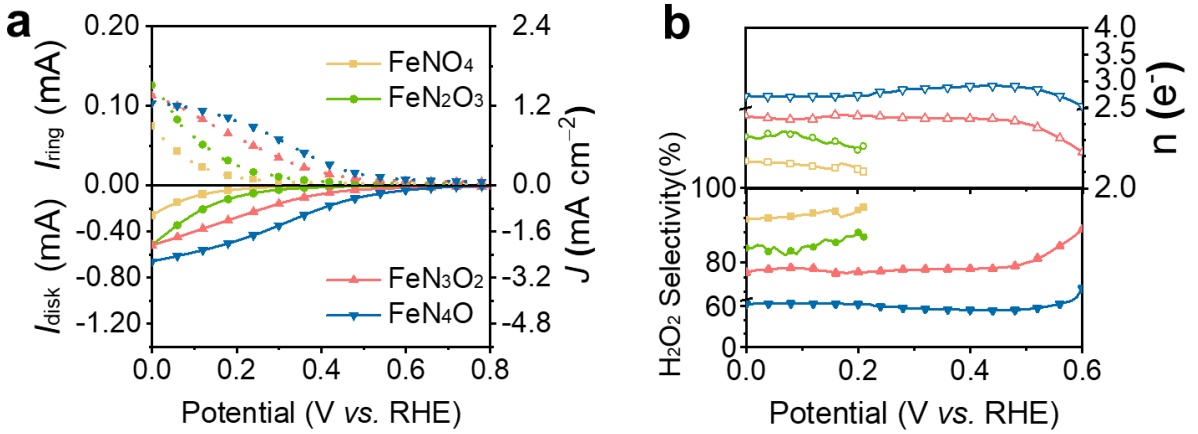

Supplementary Figure 33 | ORR performance of $FeN_{5-x}O_x$ catalysts in neutral electrolyte. **a**, ORR polarization curve measured by a rotating ring-disk electrode at 1600 rpm in O_2-saturated 0.1 M PBS (*p*H=7.2 ± 0.1). **b**, Calculated ORR electron transfer number and H_2O_2 selectivity of $FeN_{5-x}O_x$ catalysts at 0–0.6 V *vs*. RHE.

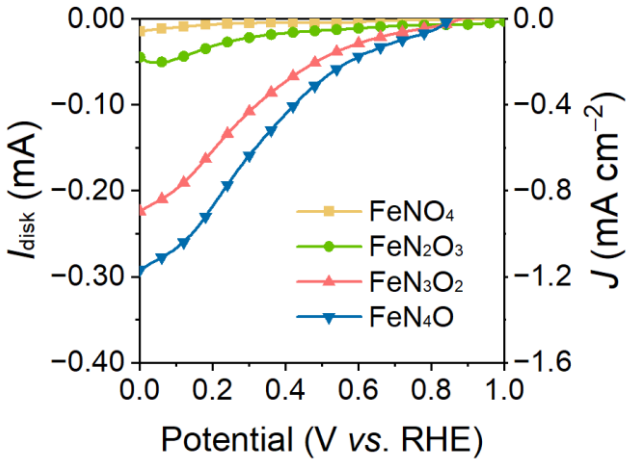

Supplementary Figure 34 | Peroxide reduction reaction for $FeN_{5-x}O_x$ catalysts. Reduce current measured by a rotating ring-disk electrode at 1600 rpm in N_2-saturated 0.1 M KOH (*p*H=13.0 ± 0.1) containing 3.5 mM H_2O_2.

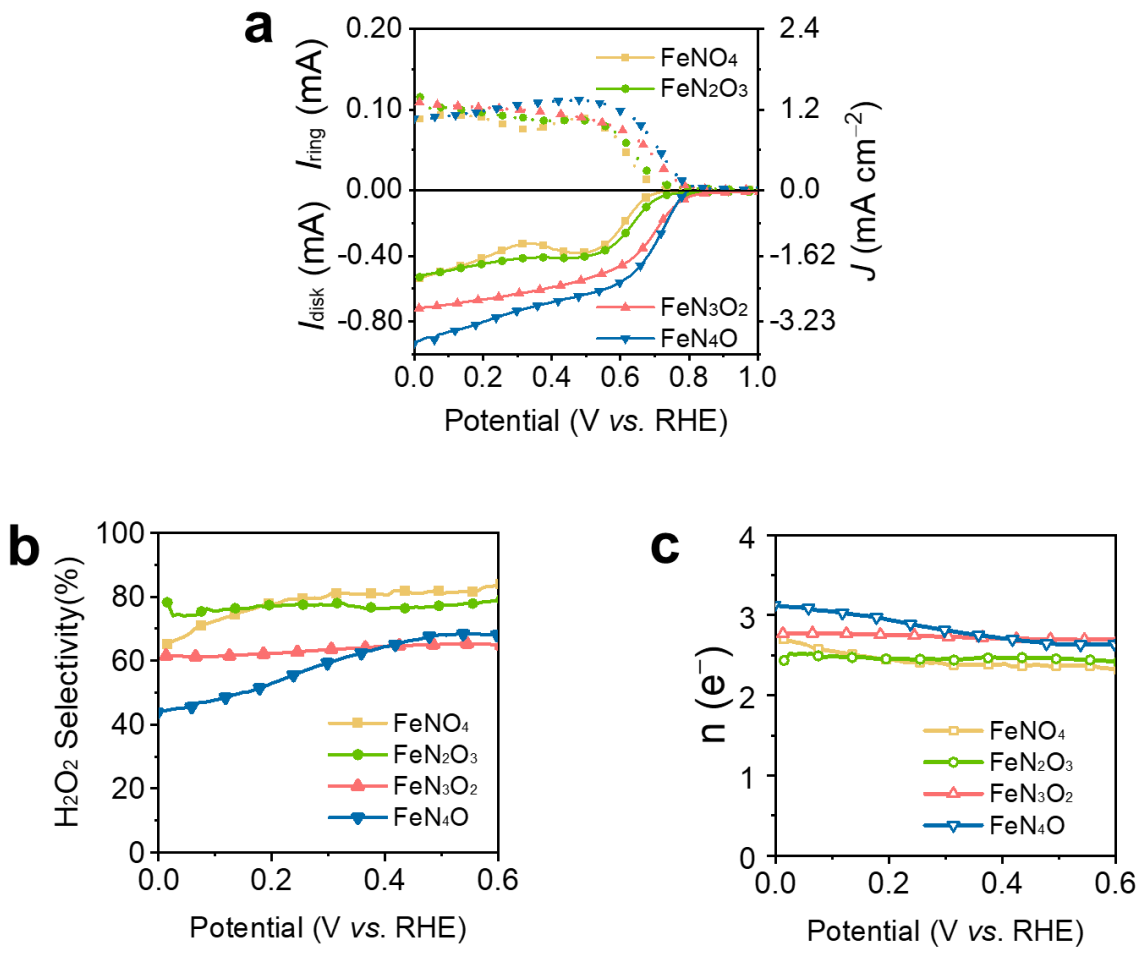

Supplementary Figure 35 | ORR performance of $FeN_{5-x}O_x$ catalysts. a, ORR polarization curve measured by a rotating ring-disk electrode at 1600 rpm in O_2-saturated 0.1 M KOH (*p*H=13.0 ± 0.1). The absolute mass loading of $FeN_{5-x}O_x$ catalysts on electrode was 0.4 mg cm^{-2}. **b,** Calculated ORR electron transfer number and **c,** H_2O_2 selectivity of $FeN_{5-x}O_x$ catalysts at 0–0.6 V *vs*. RHE.

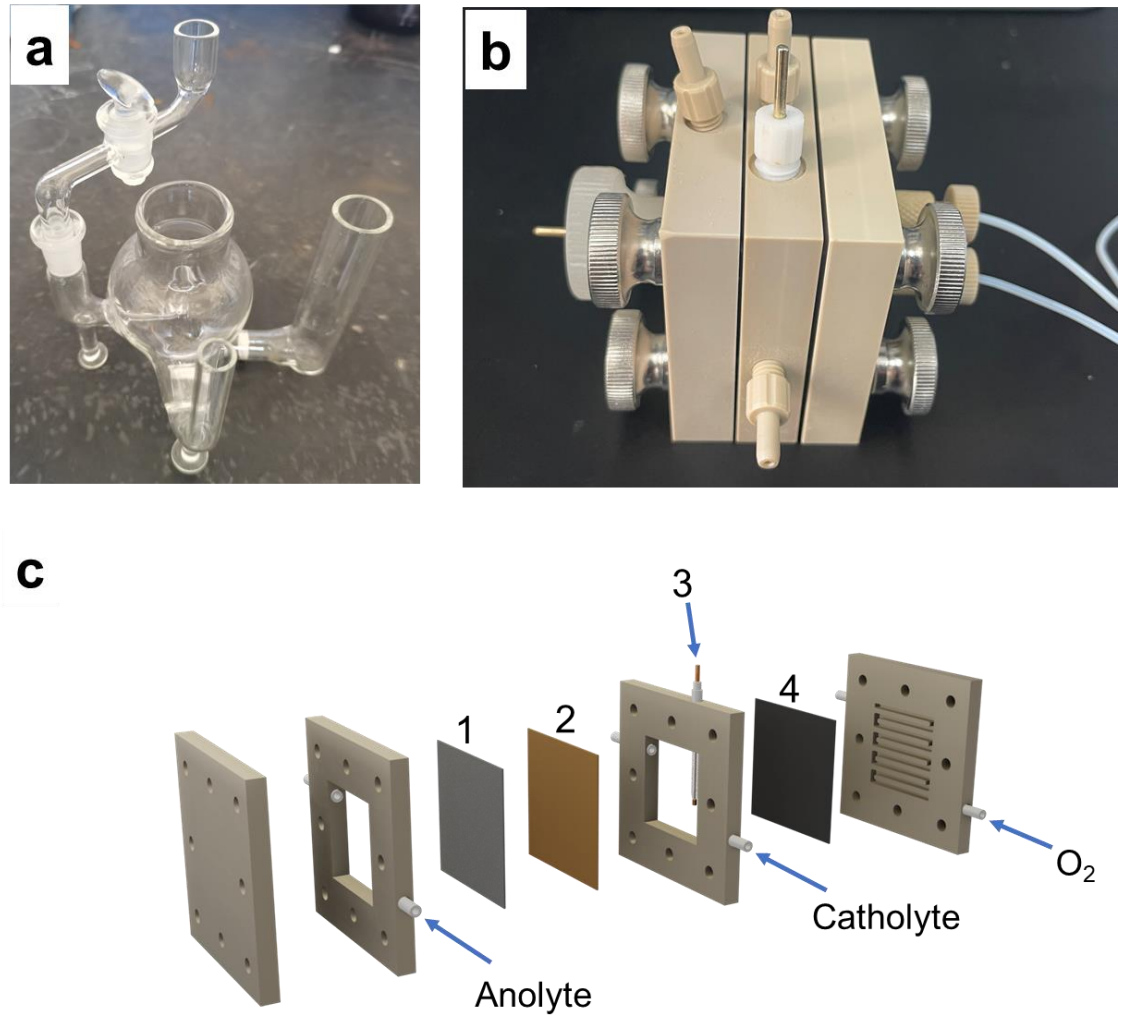

Supplementary Figure 36 | Electrochemical cell configurations for ORR testing. a, Custom three-electrode cell for rotating ring-disk electrode measurements. **b,** Flow Cell Setup. **c,** The disassembly diagram of the flow cell components. (1) Nickel foam, (2) Anion exchange membrane, (3) Ag|AgCl electrode, (4) Gas diffusion electrode.

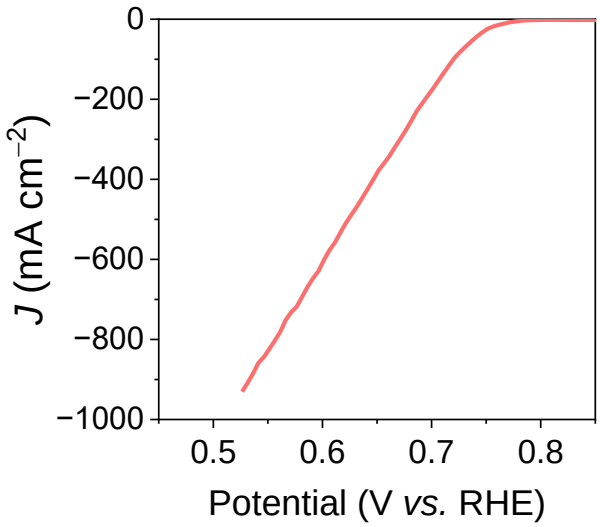

Supplementary Figure 37 | Polarization curve of FeN_3O_2 catalyst on the gas-diffusion electrode in 1 M KOH (*p*H=13.0 ± 0.1)**.**

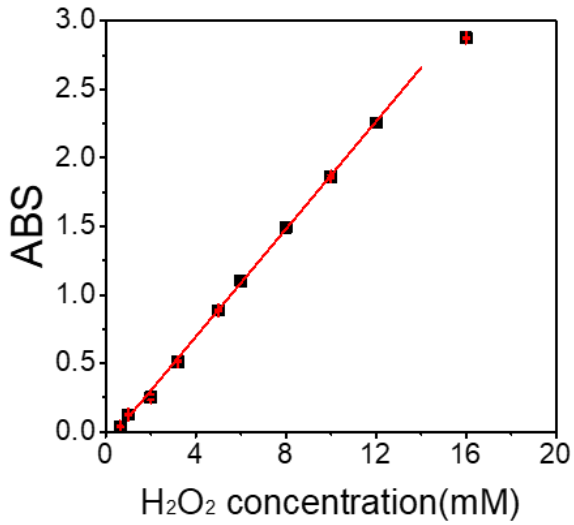

Supplementary Figure 38 | Colorimetric method quantified H_2O_2 concentration. To ensure the accuracy of measured H_2O_2 concentration, the sample was diluted to an absorbance intensity between 0.5 to 2.00.

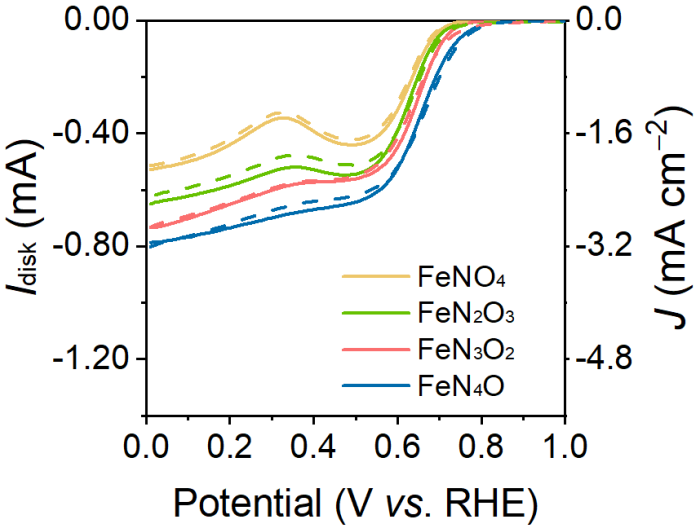

Supplementary Figure 39 | The ORR currents catalyzed by $FeN_{5-x}O_x$ catalysts after potassium thiocyanate poisoning. ORR currents measured by a rotating ring-disk electrode at 1600rpm in O_2-saturated 0.1 M KOH (*p*H=13.0 ± 0.1) contained (dashed line) and without(solid line) 10 mM KSCN.

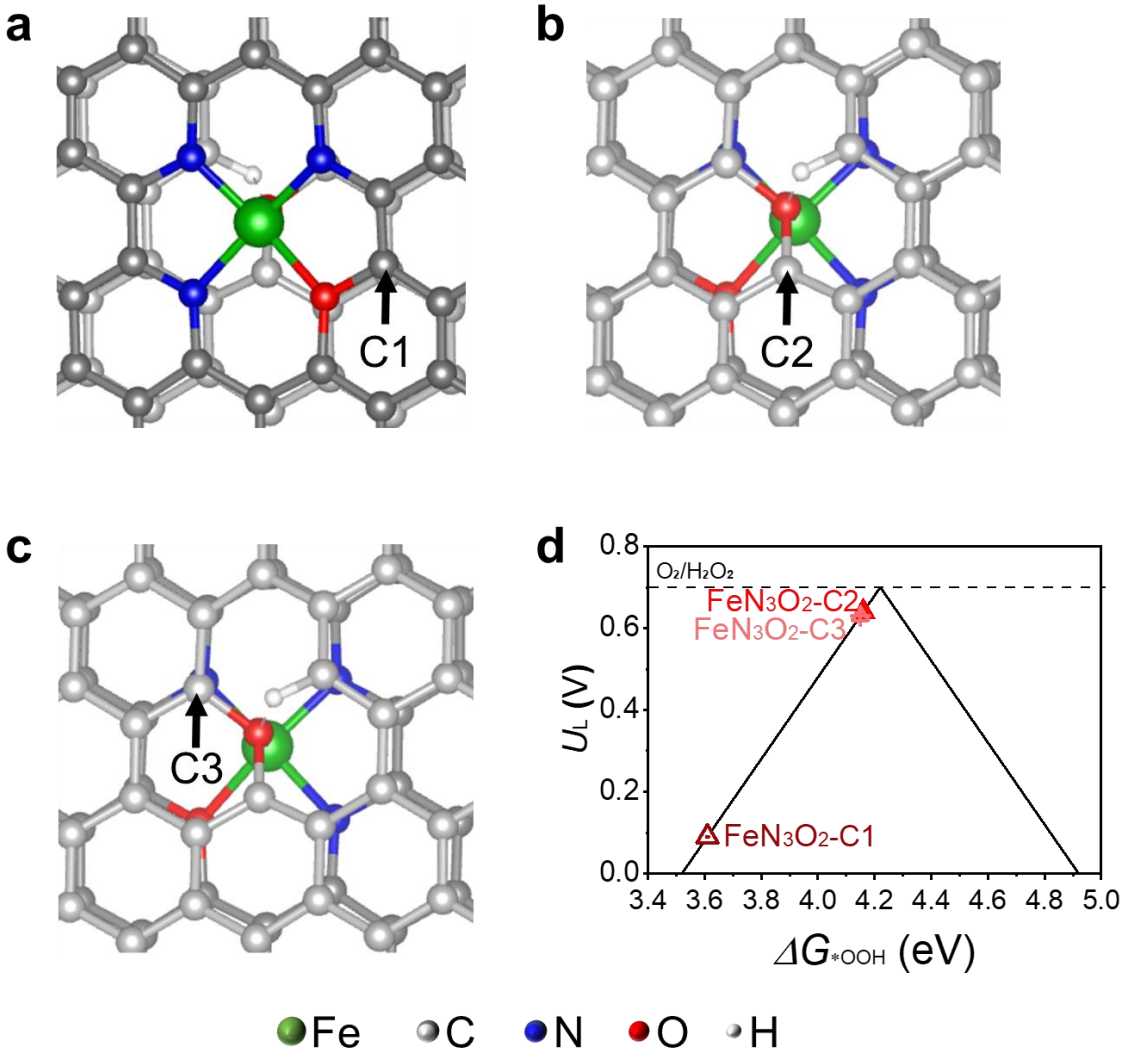

Supplementary Figure 40 | Computed activity volcano plots of different reactive sites in FeN_3O_2 motif catalyzing the $2e^-$ ORR. a, The speculated reactive site of C1. **b,** The speculated reactive site of C2. **c,** The speculated reactive site of C3. The speculated reactive site in FeN_3O_2 was annotated with arrow. **d,** The corresponding volcano points of different reactive sites in FeN_3O_2 motif catalyzing the $2e^-$ ORR.

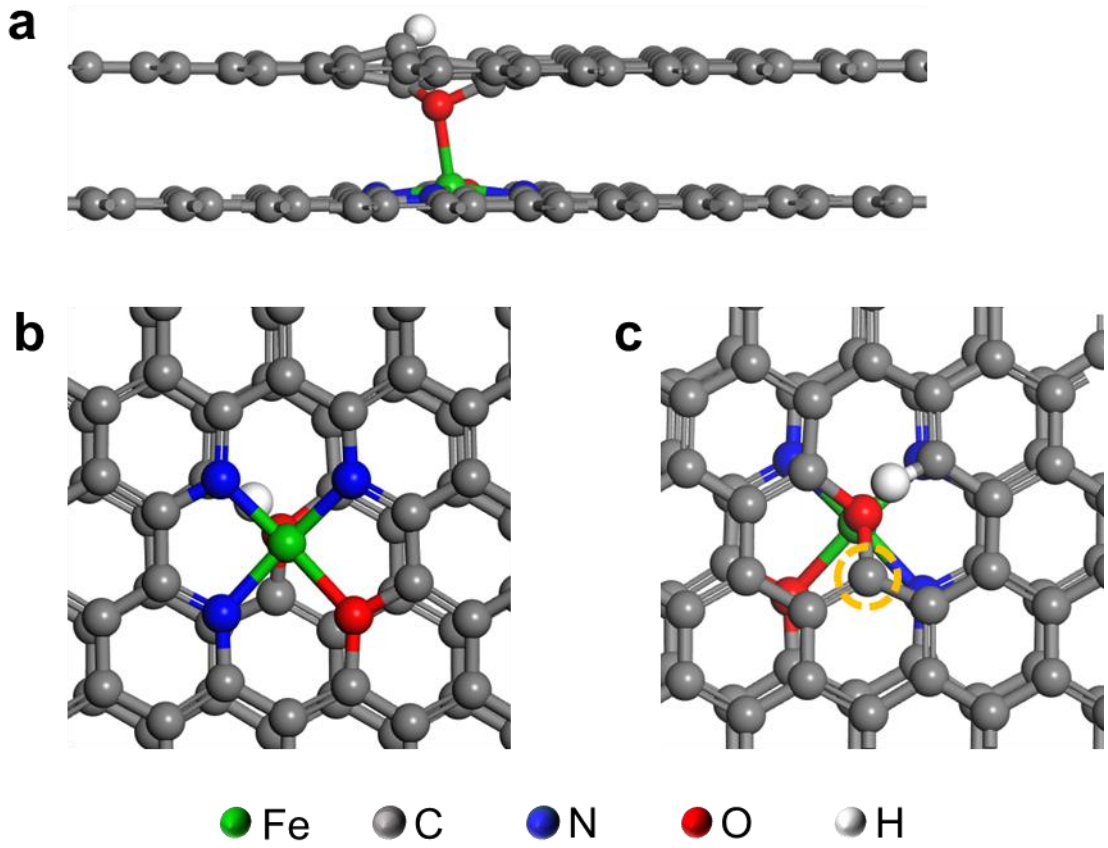

Supplementary Figure 41 | The local structure of FeN_3O_2. The catalytic site of FeN_3O_2 was indicated by the yellow circle. **a,** Left view. **b,** Top view. **c,** Elevation view.

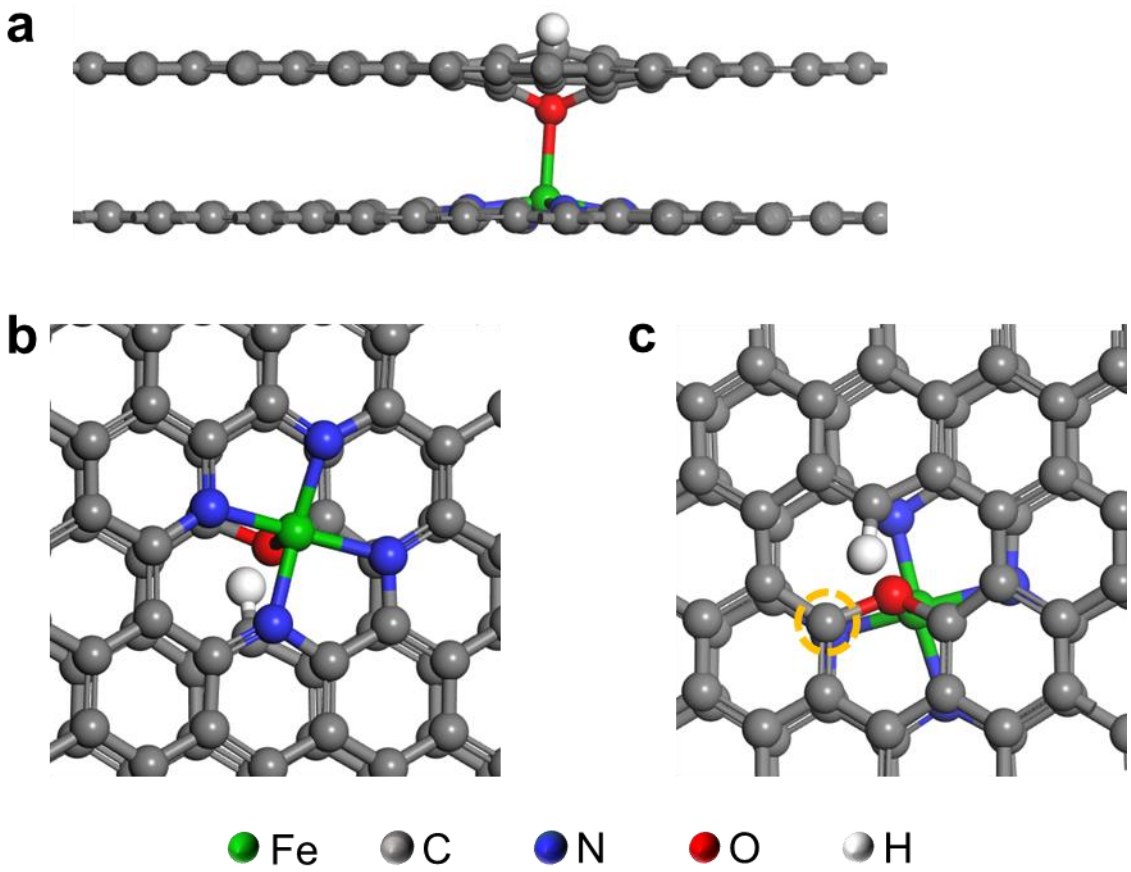

Supplementary Figure 42 | The local structure of FeN_4O. The catalytic site of FeN_4O was indicated by the yellow circle. **a,** Left view. **b,** Top view. **c,** Elevation view.

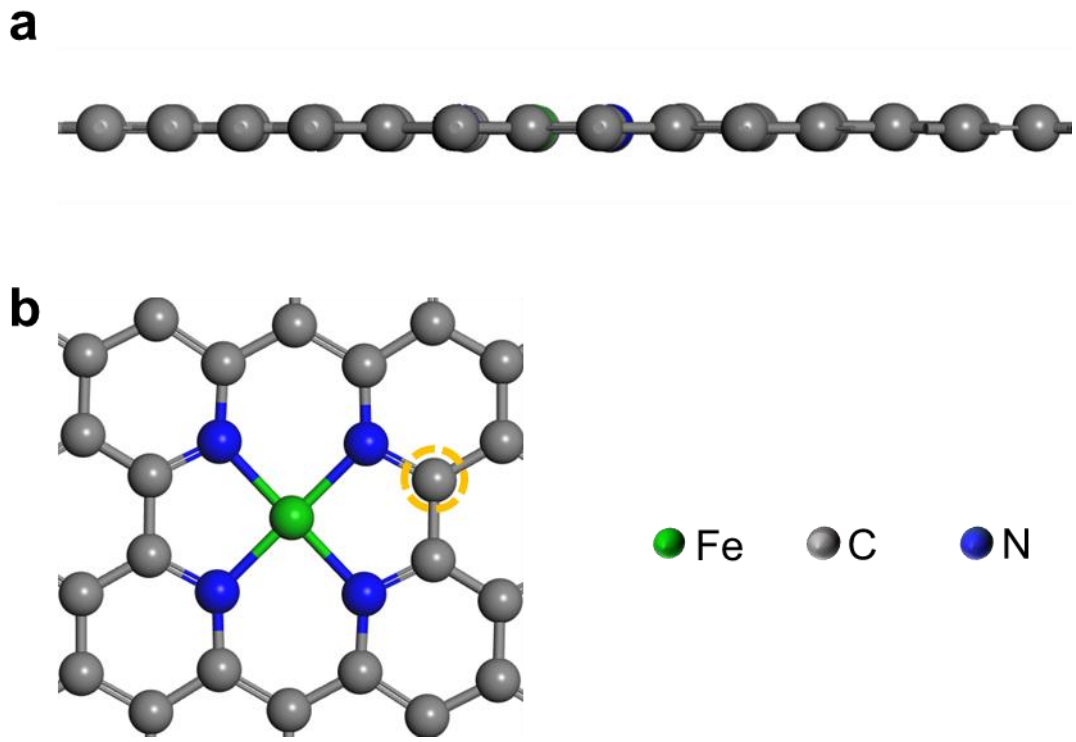

Supplementary Figure 43 | The local structure of FeN_4. The catalytic site of FeN_4 was indicated by the yellow circle. **a,** Left view. **b,** Top view.

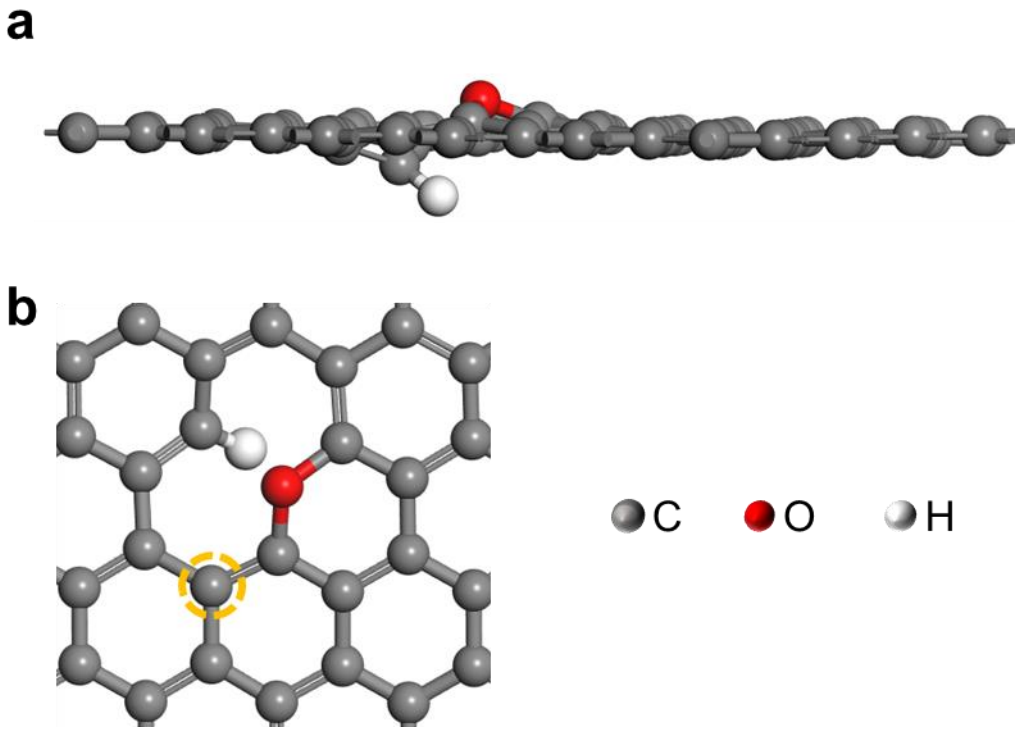

Supplementary Figure 44 | The local structure of O/C. The catalytic site of O/C was indicated by the yellow circle. **a,** Left view. **b,** Top view.

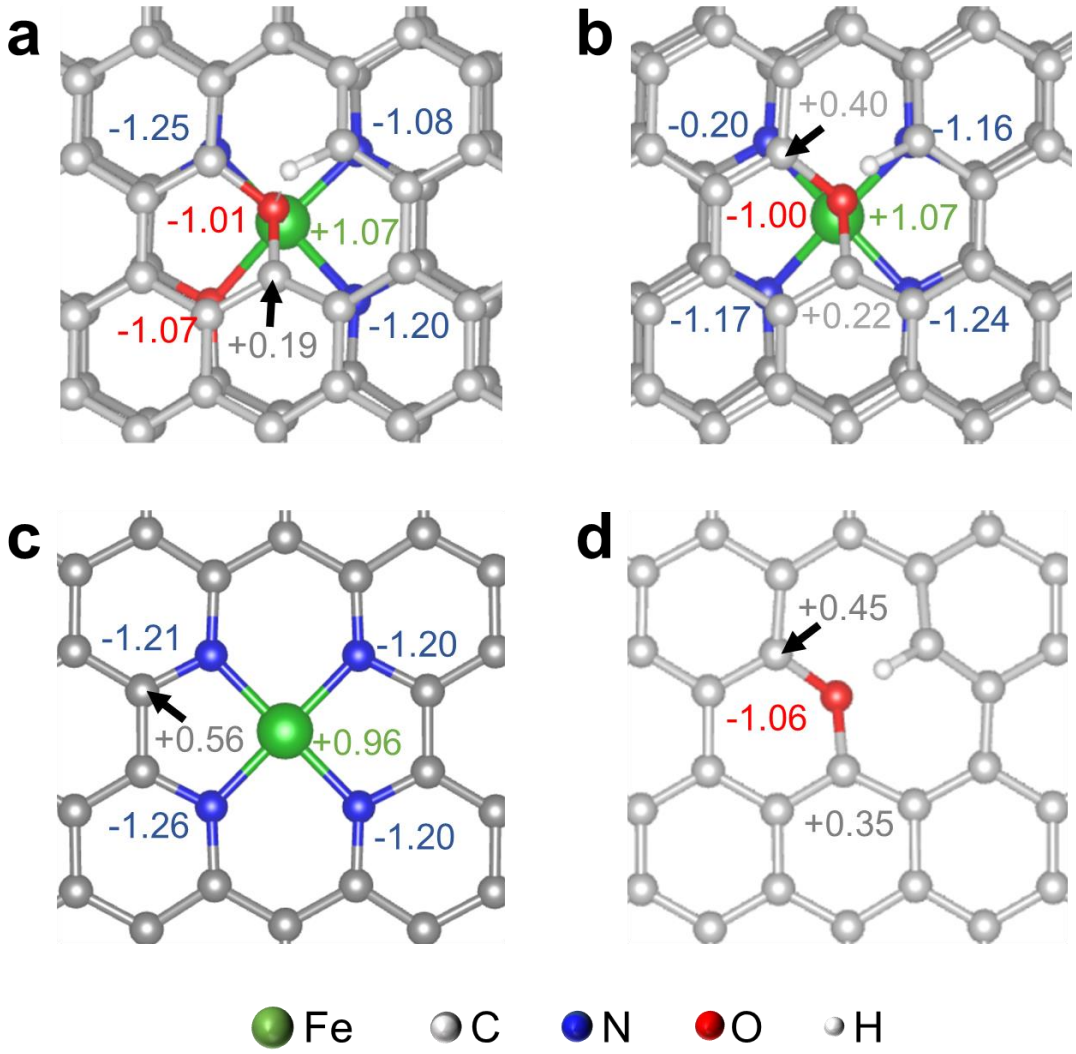

Supplementary Figure 45 | The differential charge densities of a, FeN_3O_2, b, FeN_4O, c, FeN_4, and d, O/C motif. The corresponding color values next to atoms represent their valence electron number.

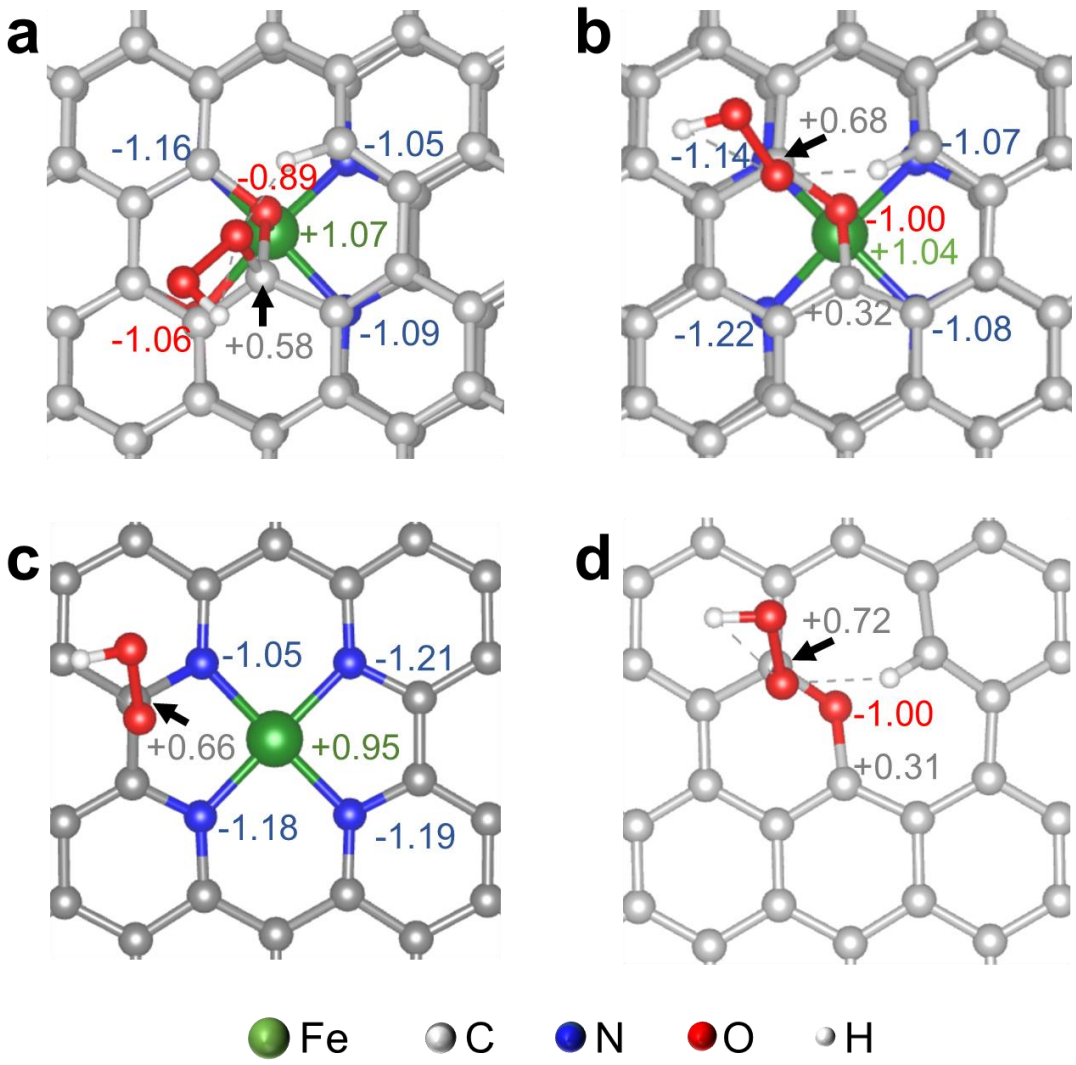

Supplementary Figure 46 | The differential charge densities of a, FeN_3O_2, b, FeN_4O, c, FeN_4, and d, O/C motif after ∗OOH adsorption. The corresponding color values next to atoms represent their valence electron number.

Supplementary Table 1 | Microbial information and cultivated condition.

Microorganism	16s/18s sequence	Medium	Cultivated condition
Escherichia coli	EU784137.1	Luria-Bertani medium[1] (*p*H = 7.0 ± 0.2): Tryptone, 10.0 g L^{-1}; sodium chloride, 10.0 g L^{-1}; yeast extract, 5.0 g L^{-1}.	30 °C, 150 rpm, 16 h
Shewanella oneidensis	MN900682.1		
Halomonas titanicae	NG063315.1		
Pseudomonas aeruginosa	NR112116.2		
Cupriavidus necator	NR043403.1		
Bacillus thuringiensis	NR116997.1		
Bacillus subtilis	NR074798.1		
Bacillus pumilus	JQ695937.1		
Saccharomyces cerevisiae	NR044719.2		
Lactobacillus acidophilus	NR043182.1	MRS medium[2] (*p*H = 7.0 ± 0.2): Glucose, 20.0 g L^{-1}; tryptone, 10.0 g L^{-1}; beef extract desicxant, 8.0 g L^{-1}; yeast extract, 4.0 g L^{-1}; potasium hydrogen phosphate, 2.0 g L^{-1}; diammonium citrate, 2.0 g L^{-1}; sodium acetate, 5.0 g L^{-1}; magnesium sulfate, 0.2 g L^{-1}, manganese chloride, 0.05 g L^{-1}; polysorbate-80, 1.0 mL L^{-1}.	37 °C, 0 rpm, 48 h
Eubacterium limosum	NR026078.1	Customized medium (*p*H = 7.0 ± 0.2): Yeast extract, 20.0 g L^{-1}; sodium DL-lactate, 7.7 mL L^{-1}; tryptone, 5.0 g L^{-1}; potassium dihydrogen phosphate, 2.0 g L^{-1}; cysteine, 10.0 g L^{-1};	30 °C, 150 rpm, 16 h
Bacillus pumilus(Fe−)		Iron-free minimal medium[3] (*p*H = 7.5 ± 0.2): Ammonium sulfate, 2.0 g L^{-1}; potassium chloride, 2.0 g L^{-1}; magnesium sulfate heptahydrate, 1.0 g L^{-1}; sodium acetate, 1.0 g L^{-1}; 50 mM tri(hydroxymethyl) amino methane hydrochloride (*p*H = 7.5) supplemented with 2.2 g L^{-1} manganese sulphate tetrahydrate, 2.0 g L^{-1} glucose, 0.7 g L^{-1} glutamate, 0.2 g L^{-1} potassium dihydrogen phosphate, 0.2 g L^{-1} calcium chloride, and 10 μL L^{-1} biotic.	30 °C, 150 rpm, 16 h

Supplementary Table 2 | Estimates of evolutionary divergence between sequences

		1	2	3	4	5	6	7	8	9	10
1.	*Escherichia coli*		0.0202	0.0269	0.0246	0.0304	0.0402	0.0402	0.0371	0.0369	0.0394
2.	*Shewanella oneidensis*	0.1635		0.0259	0.0248	0.0278	0.0398	0.0389	0.0355	0.0365	0.0388
3.	*Halomonas titanicae*	0.2606	0.2407		0.0254	0.0296	0.0394	0.0374	0.0356	0.0361	0.0375
4.	*Pseudomonas aeruginosa*	0.2225	0.2343	0.2212		0.0277	0.0380	0.0377	0.0365	0.0357	0.0377
5.	*Cupriavidus necator*	0.3350	0.2970	0.2894	0.2759		0.0397	0.0377	0.0360	0.0351	0.0377
6.	*Eubacterium limosum*	0.4700	0.4608	0.4445	0.4439	0.4690		0.0330	0.0304	0.0300	0.0317
7.	*Lactobacillus acidophilus*	0.4798	0.4513	0.4133	0.4535	0.4524	0.3712		0.0271	0.0274	0.0292
8.	*Bacillus thuringiensis*	0.4310	0.4156	0.3911	0.4274	0.4395	0.3139	0.2470		0.0168	0.0191
9.	*Bacillus subtilis*	0.4502	0.4351	0.3990	0.4253	0.4259	0.3005	0.2481	0.1098		0.0130
10.	*Bacillus pumilus*	0.4555	0.4427	0.4027	0.4179	0.4265	0.3212	0.2683	0.1320	0.0631	
11.	*Saccharomyces cerevisiae*	1.4445	1.3765	1.3994	1.4012	1.3391	1.2942	1.4067	1.3615	1.3911	1.3810

The number of amino acid substitutions per site from between sequences were shown below the diagonal.. Standard error estimate(s) were shown above the diagonal. Analyses were conducted using the Poisson correction model[4]. This analysis involved 11 amino acid sequences. The coding data was translated assuming a Standard genetic code table. All ambiguous positions were removed for each sequence pair (pairwise deletion option). There were a total of 503 positions in the final dataset. Evolutionary analyses were conducted in MEGA11[5].

Supplementary Table 3 | The BET surface area and pore distribution of *Bacillus pumilus-derived carbon materials* obtained at different tempretures.

	450°C	500°C	600°C	700°C	900°C
BET Surface Area (m^2 g^{-1})	33.09	35.80	88.43	112.41	452.73
Single point adsorption total pore volume of pores (cm^2 g^{-1})	0.081	0.076	0.068	0.130	0.348
t-Plot micropore volume (cm^2 g^{-1})	0.0004	0.0044	0.0307	0.0247	0.1346
Total pore volume of mesopores and macropores (cm^2 g^{-1})	0.080	0.071	0.037	0.105	0.213
BJH Desorption average pore diameter (4V/A) (nm)	32.0	31.5	16.1	13.6	11.5

The total volume of mesopores and macropores is calculated as single point adsorption total pore volume of pores minus b

Supplementary Table 4 | The fitting parameters for Fe K-edge EXAFS of *Bacillus pumilus-derived carbon materials* obtained at different tempretures using FeN_3O_2 model.

Sample	Path	CN	Reff (Å)	R (Å)	σ^2 (Å^2)	E_0 (eV)	R Factor
Without pyrolysis	Fe–N	2.3±2.5	1.93	1.89	0.000	−3.22±9.97	0.032
	Fe–O	4.2±3.0	2.09	2.01	0.001		
450°C	Fe–N	1.2±2.2	1.93	1.88	0.000	−2.95±12.31	0.009
	Fe–O	4.0±3.1	2.09	2.01	0.003		
500°C	Fe–N	2.0±1.6	1.93	1.90	0.000	−0.81±5.72	0.002
	Fe–O	3.2±2.3	2.09	2.03	0.001		
600°C	Fe–N	3.0±3.8	1.93	1.96	0.001	−4.80±10.05	0.126
	Fe–O	1.9±2.4	2.09	2.00	0.003		
700°C	Fe–N	3.4±6.4	1.93	1.98	0.002	−0.53±4.15	0.001
	Fe–O	1.4±5.0	2.09	2.06	0.005		
900°C	Fe–N	4.4±0.4	1.93	2.01	0.006	2.72±1.97	0.032

ΔE_0 was refined as a global fit parameter, returning a value of (−3 ± 1) eV. Data ranges: $2.5 \leq k \leq 10.5$ Å^{-1}, $1 \leq R \leq 2$Å. The distances for Fe–N and Fe–O were from the FEFF file of structure in Supplementary Figure 28.

Supplementary Table 5 | Free energy for O_2, H_2O and H_2.

	E (eV)	*ZPE*+*U*−*TS* (eV)	*G* (eV)
O_2	–	–	−9.77
H_2O	−14.21	0.08	−14.14
H_2	−6.75	−0.04	−6.79
H_2O_2	–	–	−17.96

In this work, free energy for O_2, H_2O and H_2 used as computed traditionally.

Supplementary References

1. Sezonov, G., Joseleau-Petit, D. & D'Ari, R. *Escherichia coli* physiology in Luria-Bertani broth. *J. Bacteriol.* **189**, 8746–8749 (2007).
2. De Man, J.C., Rogosa, M. & Sharpe, M.E. A medium for the cultivation of lactobacilli. *J. Appl. Bacteriol.* **23**, 130–135 (1960).
3. Handtke, S. et al. *Bacillus pumilus* reveals a remarkably high resistance to hydrogen peroxide provoked oxidative stress. *PLoS One* **9**, e85625 (2014).
4. Zuckerkandl, E. & Pauling, L. in Evolving genes and proteins (eds. Bryson, V. & Vogel, H.J.) 97–166 (Academic Press, 1965).
5. Tamura, K., Stecher, G. & Kumar, S. MEGA11: molecular evolutionary genetics analysis version 11. *Mol. Biol. Evol.* **38**, 3022–3027 (2021).